Electronic
Research Archive

https://www.aimspress.com/journal/era

ERA, 34(5): 3350–3379.
DOI: 10.3934/era.2026151
Received: 26 February 2026
Revised: 30 March 2026
Accepted: 09 April 2026
Published: 17 April 2026

Research article

Spatiotemporal dynamics of a facultative predation-parasitism model for Pine Wilt Disease with top-hat nonlocal perception

Bowei Xv and Yuting Ding*

Department of Mathematics, Northeast Forestry University, Harbin 150040, China

* **Correspondence:** Email: yuting840810@163.com.

Abstract: *Sclerodermus guani* is a facultative natural enemy with dual functional responses of predation and parasitism, which has been widely used in the biological control of *Monochamus saltuarius*, the vector insect of Pine Wilt Disease (PWD). However, most existing studies treat its predation and parasitism behaviors in isolation and ignore the synergistic effect of the dual functions. Based on this, we innovatively construct a facultative predation-parasitism reaction-diffusion model with top-hat nonlocal perception, dual predation-parasitism functional responses, and parasitic time delay, and we systematically analyze the spatiotemporal dynamic behaviors of the model. Theoretical analysis shows that, in the absence of time delay, the nonlocal perception intensity η and perception range R can induce local over-predation of the host by natural enemies and population collapse, forming stable spatially nonhomogeneous steady-state solutions. When the parasitic time delay exceeds the critical value, the delay effect leads to periodic population oscillation. The synergistic effect of nonlocal perception and time delay induces Turing-Hopf bifurcation, presenting complex spatiotemporally coupled patterns. Numerical simulations based on parameters with realistic biological backgrounds verify the correctness of the theoretical analysis, and intuitively demonstrate the dynamic modes corresponding to different parameters, including local asymptotic stability, stable spatially nonhomogeneous steady-state solutions, and spatially nonhomogeneous periodic solutions. The results reveal the regulation mechanism of top-hat nonlocal perception and parasitic time delay on the spatiotemporal dynamics of the *Monochamus saltuarius*-*Sclerodermus guani* system. They not only enrich the spatiotemporal dynamics theory of facultative predation-parasitism systems, but also provide a quantitative mathematical basis for optimizing the release timing and release strategy of *Sclerodermus guani* in prevention and control as well as lay a theoretical foundation for the biological control of PWD.

Keywords: Pine Wilt Disease; facultative predation-parasitism model; top-hat nonlocal perception; dual functional responses; parasitic time delay; Turing-Hopf bifurcation

1. Introduction

Pine Wilt Disease (PWD) is a devastating pine (*Pinus* spp.) disease caused by *Bursaphelenchus xylophilus*, a nematode native to North America. Due to long-term coevolutionary resistance and tolerance in native pines, it causes no large-scale damage there, but has invaded Japan, China, South Korea, Portugal and Spain via human activities like timber imports, posing a severe threat to local pine populations lacking adaptive defenses and is listed as a key quarantine target in over 50 countries [1].

The dispersal capability of *Bursaphelenchus xylophilus* itself is extremely limited. Its effective spread within pine forest ecosystems is highly dependent on vector insects, primarily beetles of the species *Monochamus alternatus* and *Monochamus saltuarius* [2]. As illustrated in Figure 1, the transmission mechanism operates as follows [3]. Adult *Monochamus alternatus* and *Monochamus saltuarius* vectors deposit eggs within bark crevices of pine trees. Larvae subsequently bore into the xylem upon hatching. *Bursaphelenchus xylophilus* simultaneously invades the host through these wounds, utilizing pine parenchyma cells or associated fungi as nutritional sources for population proliferation. The critical transmission event occurs immediately prior to beetle pupation and emergence: large numbers of nematodes aggregate and enter the developing adult's tracheal system. When nematode-carrying adult vectors fly to healthy pines for maturation feeding on young branch bark, *Bursaphelenchus xylophilus* successfully infects new hosts through the resulting feeding wounds.

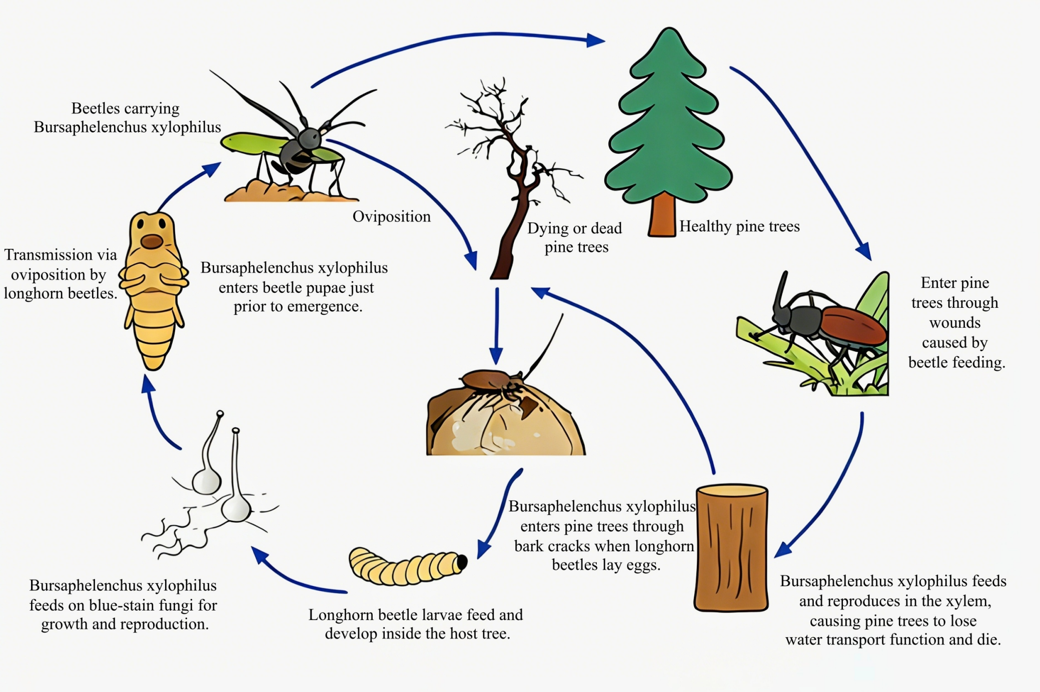

Figure 1. Transmission mechanism of PWD.

Following infection by *Bursaphelenchus xylophilus*, susceptible pine species exhibit diagnostic pathological symptoms as shown in Figure 2(a): progressive discoloration of needles from chlorotic yellow to necrotic reddish-brown, systemic wilting with characteristic drooping morphology, and cessation of resin exudation. To clearly distinguish between infested areas and healthy areas, we plotted the corresponding heatmap, see Figure 2(b). It can be clearly observed from the heatmap that the infested areas exhibit a characteristic distribution pattern with a combination of strip-shaped and dot-shaped distributions. This physiological deterioration significantly enhances the survival rate of *Monochamus* eggs and larvae, thereby increasing the stand's attractiveness to *Monochamus* vector beetles and establishing a strong positive feedback loop. This mechanism greatly accelerates the spread and destructive rate of the disease within pine forest ecosystems, a process metaphorically referred to as a "forest fire without smoke".

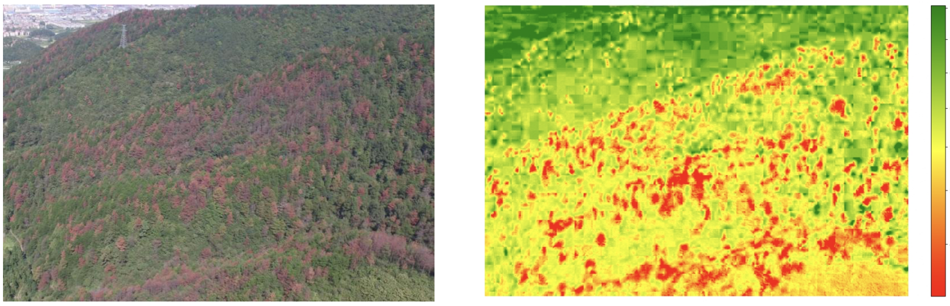

(a) **(b)**

Figure 2. Infected pine trees and spatial distribution heatmap.

Given the high dependence of PWD transmission on vector insects, current control strategies primarily focus on managing *Monochamus* vector populations to disrupt the disease transmission chain. However, *Monochamus* beetles are stem-boring pests with concealed life cycles, spending most of their larval development phase tunneling inside the wood. Their adult emergence period is asynchronous and protracted, presenting significant challenges for population control. Traditional physical control methods and chemical pesticide applications were the main early approaches, but physical control is slow-acting and costly, while chemical control carries non-negligible environmental pollution risks. In recent years, environmentally-friendly biological control technologies, such as the release of natural enemies and the utilization of pathogenic microorganisms, have demonstrated significant potential and undergone rapid development in regulating *Monochamus* vector populations [4].

In the biological control practice targeting the vector longhorn beetles of pine wilt disease, determining the optimal timing and quantity of natural enemy releases to maximize control efficacy while minimizing costs is a core optimization problem. Mathematical ecology provides a theoretical framework and quantitative tools for analyzing such complex spatiotemporal dynamics. The modeling of predator-prey interactions originated from the classical Lotka-Volterra model, and Holling's functional response theory remedied the defects of the classical model that ignored predator handling time and energy conversion efficiency [5]. Subsequent studies clarified the key role of spatial heterogeneity in population dynamics, promoted the development of modeling based on reaction-diffusion equations, and laid a foundation for analyzing the spatial distribution and diffusion mechanisms of populations [6]. As research advances, the characterization of animal movement in models has gone beyond simple physical diffusion. Accordingly, incorporating behavioral mechanisms such as taxis, memory, and nonlocal effects has become an inevitable trend [7–11]. Relevant studies have demonstrated that these mechanisms can significantly change the stability of predator–prey systems and induce distinct spatiotemporal patterns and various bifurcation phenomena [12–14].

Notably, individual animals complete complex behavioral decisions by integrating environmental chemical and physical signals through perception, and this cognitive process mediates key survival behaviors such as predator avoidance and prey tracking. In recent years, perception mechanisms have become a research hotspot in this field. Song et al. [15] established a diffusive consumer-resource model incorporating nonlocal resource perception, systematically analyzed the impact of different perception kernel functions on system stability, and found that this mechanism can drive the generation of striped patterns, oscillatory patterns, and spatiotemporal chaos. Li et al. [16, 17] focused on the biological control of *Monochamus alternatus* by *Dastarcus helophoroides*, explored the impact of nonlocal perception on the spatiotemporal transmission pattern of pine wilt disease, and clarified the joint effect of perception scale and time delay on system stability for the top-hat kernel function. They found that the interaction between the two can induce Turing-Hopf bifurcation, providing a practical application background for the theoretical analysis of Song et al. [15].

Our study focuses on optimizing the biological control strategy against the vector beetle *Monochamus saltuarius*. Zheng et al. [18] pointed out that the main parasitic natural enemies currently used in practical control of wood-boring pests, such as longhorn beetles, are *Sclerodermus guani* and *Dastarcus helophoroides*. Among them, studies on the population dynamics of *Dastarcus helophoroides* in controlling longhorn beetles are relatively abundant, while studies on the dynamic mechanism of *Sclerodermus guani*, especially against *Monochamus saltuarius*, are relatively insufficient. The work of Yang et al. [19] revealed that female *Sclerodermus guani* wasps exhibit a dual lethal mechanism against their hosts: Oviposition parasitism and lethal stinging and feeding to obtain nutrition for oviposition. Their functional response analysis showed that the predation behavior of *Sclerodermus guani* follows the Holling type II functional response, while the parasitism behavior conforms to the Holling type I functional response. Zheng et al. [20] further confirmed that *Sclerodermus guani* displays a similar behavioral pattern with the above dual lethal mechanism when attacking *Monochamus saltuarius* larvae.

The spatial host-location process of *Sclerodermus guani* is also strongly affected by environmental heterogeneity and its own perception range. Existing studies have shown that pine trees infested by *Monochamus saltuarius* release specific volatile chemical signals that attract *Sclerodermus guani*. After entering a sufficiently small spatial range, *Sclerodermus guani* can further locate hosts by detecting volatile compounds in the frass of beetle larvae. However, the physical diffusion of chemical signals in forest habitats is strongly constrained: Signals may be diluted by atmospheric turbulence below the detection threshold of *Sclerodermus guani*, or diffusion may fail due to disturbances in the canopy microclimate. According to Fagan et al. [21], this scenario corresponds to a step-function truncation of perception intensity beyond a fixed radius. That is, the perception ability of *Sclerodermus guani* is constant within the radius R, but immediately vanishes beyond this threshold. Therefore, we adopt a top-hat kernel function to characterize the nonlocal resource perception of *Sclerodermus guani*.

However, continuous decaying kernels, such as the Gaussian kernel, fail to accurately describe this biological mechanism. The Gaussian kernel assumes that the perception intensity of parasitoids decreases smoothly and continuously with distance, and theoretically maintains a weak perceptual ability even at an infinite spatial distance. This contradicts the realistic feature that chemical signals in forest environments possess a definite detection threshold. When volatile signals are diluted by atmospheric turbulence or disturbed by canopy microclimate, their concentration will drop below the olfactory detection limit of *Sclerodermus guani*. Consequently, the parasitoid loses its host perception abruptly rather than undergoing gradual attenuation. In contrast, the step-truncation property of the top-hat kernel perfectly matches such a threshold effect: The perception ability remains uniform within a fixed radius and vanishes completely once exceeding the threshold. Moreover, this modeling framework is highly consistent with the mathematical description of host-location behaviors of natural enemies proposed by Fagan et al. in previous literature [21].

Most existing relevant studies have analyzed the pest control efficacy of *Sclerodermus guani* in isolation, focusing solely on its single predation or parasitism behavior, while ignoring the synergistic control effect of the two types of functional responses. Meanwhile, for the *Sclerodermus guani-Monochamus saltuarius* system, few studies have focused on the regulation mechanism of the coupling effect between top-hat nonlocal perception behavior and parasitic time delay on the spatiotemporal dynamics of the system, resulting in the inability of existing models to accurately characterize the realistic evolution law of population patterns in field pine forest ecosystems.

In summary, the following facultative predation-parasitism model for *Sclerodermus guani* and *Monochamus saltuarius* has been constructed, incorporating top-hat nonlocal resource perception, featuring both predation and parasitism functional responses:

$$\begin{cases} \dfrac{\partial u}{\partial t} = d_1\Delta u + ru\left(1-\dfrac{u}{K}\right) - \alpha uv - \dfrac{\gamma uv}{1+\gamma uh} - \xi u, & x \in (-\infty,+\infty), t>0, \\ \dfrac{\partial v}{\partial t} = d_2\Delta v - d_3 v - \eta(v\, p_x)_x + \delta\alpha u(x,t-\tau)v + \dfrac{\beta\gamma uv}{1+\gamma uh}, & x \in (-\infty,+\infty), t>0, \\ u(-L,t) = u(L,t), \quad u_x(-L,t) = u_x(L,t), \quad t>0, \\ v(-L,t) = v(L,t), \quad v_x(-L,t) = v_x(L,t), \quad t>0, \end{cases} \tag{1.1}$$

where $u(x,t)$ and $v(x,t)$ describe the density of the prey and predator at position x and time t, respectively; d_1 and d_2 are the diffusion coefficients of *Monochamus saltuarius* and *Sclerodermus guani*, respectively; Δ is the Laplacian operator; d_3 is the natural mortality rate of *Sclerodermus guani*; r is the intrinsic growth rate of *Monochamus saltuarius*; K is the environmental carrying capacity of *Monochamus saltuarius*; h is the handling time of *Sclerodermus guani*; ξ is the suppression efficacy of physical control methods; τ is the parasitic time delay; η is the perceptual diffusion coefficient of *Sclerodermus guani*; α is the parasitic efficiency of *Sclerodermus guani* on *Monochamus saltuarius*; γ is the predation efficiency of *Sclerodermus guani* on *Monochamus saltuarius*; β is the energy conversion efficiency for predation; and δ is the energy conversion efficiency for parasitism. All parameters in the system are positive constants. We use periodic boundary conditions. Moreover,

$$p_x = M_R * u = \int_\Omega M_R(x-y)u(y,t)dy,$$

and $M_R(x-y)$ is chosen as the top-hat function as follows:

$$M_R(x-y) = \begin{cases} \frac{1}{2R}, & -R \le x \le R, \\ 0, & \text{otherwise.} \end{cases}$$

The paper is organized as follows. In Section 2, we first analyze the existence conditions of the positive equilibrium. Then, we discuss the existence of Turing bifurcation, Hopf bifurcation, and Turing-Hopf bifurcation, with corresponding biological interpretations provided. In Section 3, we perform numerical simulations using biologically relevant parameter values from the literature to verify the validity of our theoretical results, and further propose practical control strategies for PWD based on the combined findings of theoretical analysis and numerical simulations. Finally, Section 4 presents the conclusion.

2. Stability and bifurcation analysis

By setting Eq (1.1) to zero, it is evident that the zero equilibrium point E_0 is the only trivial steady state that always exists. For the positive constant steady state $E_* = (u_*, v_*)$, u_* satisfies $\mathcal{W}(u_*) \triangleq \delta\alpha\gamma h u_*^2 + (\alpha\delta + \beta\gamma - d_3\gamma h)u_* - d_3 = 0$. Since $\Delta_1 = (\alpha\delta + \beta\gamma - d_3\gamma h)^2 + 4d_3\alpha\delta\gamma h \geq 0$, $\mathcal{W}(u_*)$ obviously admits a positive solution $u_* = \frac{-(\alpha\delta+\beta\gamma-d_3\gamma h)+\sqrt{\Delta_1}}{2\delta\alpha\gamma h}$. Correspondingly, v_* is given by $v_* = \frac{\left[r\left(1-\frac{u_*}{K}\right)-\xi\right](1+\gamma u_* h)}{\alpha+\alpha\gamma u_* h+\gamma}$.

To ensure v_* remains positive, we impose the following assumption:

$$(H_1) : 0 < \frac{-(\alpha\delta + \beta\gamma - d_3\gamma h) + \sqrt{\Delta_1}}{2\delta\alpha\gamma h} < K(1 - \frac{\xi}{r}) \text{ and } \xi < r.$$

For any constant steady state E_χ of the system, we first define

$$E_\chi = (u_\chi, v_\chi) = \begin{cases} (0, 0), & E_\chi = E_0, \\ (u_*, v_*), & E_\chi = E_*. \end{cases}$$

The characteristic equation at E_χ is given as follows:

$$\lambda^2 - \mathscr{A}_k\lambda + \mathscr{B}_k(\eta, R) = 0, \tag{2.1}$$

where

$$\begin{aligned} \mathscr{A}_k &= -(d_1 + d_2)k^2 + a_{11}, \\ \mathscr{B}_k &= d_1d_2k^4 - d_2a_{11}k^2 - \eta a_{12}v_\chi k^2\frac{\sin(kR)}{kR} - a_{12}a_{21} - a_{12}b_{21}e^{-\lambda\tau}, \end{aligned}$$

with

$$\begin{aligned} a_{11} &= -\frac{ru_\chi}{K} + \frac{\gamma^2u_\chi v_\chi h}{(1 + \gamma u_\chi h)^2}, \quad a_{12} = -\alpha u_\chi - \frac{\gamma u_\chi}{1 + \gamma u_\chi h}, \quad a_{21} = \frac{\beta\gamma v_\chi}{(1 + \gamma u_\chi h)^2}, \\ b_{21} &= \delta\alpha v_\chi. \end{aligned}$$

For the zero equilibrium point E_0, we obtain $\mathscr{A}_k = -(d_1 + d_2)k^2 < 0$ and $\mathscr{B}_k = d_1d_2k^4 > 0$. Thus, E_0 is locally asymptotically stable.

As for E_*, we consider the case $\tau = 0$ and $\eta = 0$. To ensure the local asymptotic stability of the positive steady state E_*, we require that $\mathscr{A}_k < 0$ and $\mathscr{B}_k > 0$. Since $a_{11} \geq -(d_1+d_2)k^2+a_{11}$, it suffices to impose the condition $a_{11} < 0$, which is equivalent to $K < \frac{r(1+\gamma u_* h)^2}{\gamma^2 v_* h}$. Under this condition, since $a_{12} < 0$, $a_{21} > 0$, and $b_{21} > 0$, the inequality $\mathscr{B}_k > 0$ holds, obviously. In summary, we propose the following assumption to ensure the local asymptotic stability of the positive steady state E_*:

$$(H_2) : K < \frac{r(1 + \gamma u_* h)^2}{\gamma^2 v_* h}.$$

Therefore, we have the following theorem.

Theorem 2.1. *The zero equilibrium point* E_0 *is always locally asymptotically stable.*

Theorem 2.2. *Assuming that assumptions* (H_1) *and* (H_2) *hold, when* $\eta = 0$ *and* $\tau = 0$*, the positive constant steady state* E_* *of system* (1.1) *is locally asymptotically stable.*

Remark 2.1. *The proof of the well-posedness of the solution to this system is similar to the method employed by Song et al. [15].*

Remark 2.2. *According to Li et al. [17], we have* $\lim_{R\to 0^+} M_R(x) = \delta(x)$ *and* $\lim_{R\to 0^+}\int_\Omega M_R(x-y)u(y,t)\,dy = u(x,t)$*. This indicates that the top-hat kernel function degenerates into the Dirac delta function in the limit.*

Next, we perform the bifurcation analysis of the system (1.1). We select η and R as the Turing bifurcation parameters and τ as the Hopf bifurcation parameter.

2.1. Turing bifurcation

First, we consider the case when $\tau = 0$ and $\eta > 0$. Since assumption (H_2) holds, $\mathscr{A}_k < 0$ remains valid, and we focus our analysis on $\mathscr{B}_k$. When $k = 0$, $\mathscr{B}_0 > 0$ still holds. For $k > 0$, setting $\mathscr{B}_k = 0$, we obtain

$$\frac{\sin(kR)}{kR} = \frac{1}{\eta v_* a_{12}}\left(d_1d_2k^2 - d_2a_{11} - \frac{a_{12}b_{21} + a_{12}a_{21}}{k^2}\right). \tag{2.2}$$

For the convenience of subsequent analysis, we define

$$f(k,R) \triangleq \frac{\sin(kR)}{kR},$$

$$g(k) \triangleq \frac{1}{\eta v_* a_{12}}\left(d_1d_2k^2 - d_2a_{11} - \frac{a_{12}b_{21} + a_{12}a_{21}}{k^2}\right).$$

Since its proof is similar to that in [15], we only present the following lemma.

Lemma 2.1. *According to* (2.2)*, let* $z_{2m-1} = k_{2m-1}R$ $(m \in \mathbb{N}_+)$*, then we have*

$$\eta^{(m)} = \frac{(2\sqrt{d_1d_2(-a_{12}b_{21} - a_{12}a_{21})} - d_2a_{11})z_{2m-1}}{a_{12}v_* \sin(z_{2m-1})}. \tag{2.3}$$

For system (1.1) *with a top-hat kernel, we have the following results.*

1) *If* $0 < \eta < \eta^{(1)}$*, then* $\mathscr{B}_k(\eta,R) > 0$ *for all* $k > 0$*, and* $R > 0$;

2) *If* $\eta = \eta^{(1)}$*, then there exist a critical value* $R_0^* > 0$ *and a positive constant* k_0^* *such that* $\mathscr{B}_{k_0^*}(\eta,R_0^*) = 0$*, while* $\mathscr{B}_k(\eta,R) > 0$ *for all* $k > 0$*, and* $R > 0$ *with* $(k,R) \neq (k_0^*,R_0^*)$;

3) *If* $\eta^{(m)} < \eta < \eta^{(m+1)}$ *for some* $m \in \mathbb{N}$*, then there exist two critical values* $0 < R^- < R^+$ *of* R *and two positive constants* $0 < k_2 < k_1$ *of* k*, such that the curves* $f(k,R)$ *and* $g(k)$ *are tangent at the point* (k_1,R^-) *or* (k_2,R^+)*. Let us now discuss this in detail.*

3a) *For* $R \in (0,R^-) \cup (R^+,+\infty)$*,* $\mathscr{B}_k(\eta,R) > 0$ *for all* $k > 0$*. Furthermore,*

  3a-1) *when* $R = R^-$*,* $\mathscr{B}_k(\eta,R) = 0$ *if and only if* $k = k_1$*, and* $\mathscr{B}_k(\eta,R) > 0$ *for all* $k \neq k_1$;

3a-2) *when* $R = R^+$, $\mathscr{B}_k(\eta, R) = 0$ *if and only if* $k = k_2$, *and* $\mathscr{B}_k(\eta, R) > 0$ *for all* $k \neq k_2$.

3b) *For* $R \in (R^-, R^+)$, *we define the following disjoint subsets of* (R^-, R^+),

$$\mathcal{R}_+ = \{R \in (R^-, R^+) \mid \mathscr{B}_k(\eta, R) > 0 \text{ for all } k > 0\},$$
$$\mathcal{R}_- = \{R \in (R^-, R^+) \mid \exists \text{ a non-empty subset } \mathcal{Z}_- \subset \mathbb{R}^+,\ \mathscr{B}_k(\eta, R) < 0 \text{ for } k \in \mathcal{Z}_-\},$$
$$\mathcal{R}_0 = \{R \in (R^-, R^+) \mid \exists \text{ a countable subset } \mathcal{Z}_0 \subset \mathbb{R}^+, \mathscr{B}_k(\eta, R) = 0 \text{ for } k \in \mathcal{Z}_0,$$
$$\mathscr{B}_k(\eta, R) > 0 \text{ for } k \notin \mathcal{Z}_0\}.$$

Then, the characteristic equation (2.1) *has the following properties.*

(i) *If* $\mathcal{R}_+ = \varnothing$ *and* $\mathcal{R}_0 = \varnothing$, *then the characteristic equation* (2.1) *has at least one positive root for all* $k \in \mathcal{Z}_-$;

(ii) *If* $\mathcal{R}_+ \neq \varnothing$, *then*

- ***(ii-a)*** *for* $R \in \mathcal{R}_+$, *all roots of the characteristic equation* (2.1) *are negative;*
- ***(ii-b)*** *for* $R \in \mathcal{R}_-$, *the characteristic equation* (2.1) *has at least one positive root for* $k \in \mathcal{Z}_-$;
- ***(ii-c)*** *for* $R \in \mathcal{R}_0$, *the characteristic equation* (2.1) *has zero roots for* $k \in \mathcal{Z}_0$ *and all other roots for* $k \notin \mathcal{Z}_0$ *are negative.*

Remark 2.3. *For* $\eta^{(1)} < \eta < \eta^{(2)}$, *it is not difficult to find that* $\mathcal{R}_+ = \varnothing$ *and* $\mathcal{R}_0 = \varnothing$. *Consequently, at this time, the characteristic equation* (2.1) *has at least one positive root for all* $R \in (R^-, R^+)$.

Based on Lemma 2.1 and Remark 2.3, we have the following theorem.

Theorem 2.3. *If* (H_1) *and* (H_2) *hold, for* $\tau = 0$, $\eta^{(m)}$ *is defined by Lemma 2.1. For the positive constant steady state* E_* *of the system* (1.1),

1) *When* $0 \leq \eta < \eta^{(1)}$, E_* *is asymptotically stable for all* $R \geq 0$;
2) *When* $\eta > \eta^{(1)}$, *we have the following results.*
   - *(a) There exist two critical values* R^- *and* R^+ *of* R *such that system* (1.1) *undergoes Turing bifurcations at both* $R = R^-$ *and* $R = R^+$, *and* E_* *is asymptotically stable for* $R \in [0, R^-) \cup (R^+, +\infty)$.
   - *(b) If* $\eta^{(1)} < \eta < \eta^{(2)}$, *then* E_* *is unstable for* $R \in (R^-, R^+)$.
   - *(c) If* $\eta^{(m)} < \eta < \eta^{(m+1)}$ *with* $m \in \mathbb{N}$, *then there are the following two cases:*
     - *(i) for* $\mathcal{R}_+ = \varnothing$ *and* $\mathcal{R}_0 = \varnothing$, E_* *is unstable for* $R \in (R^-, R^+)$;
     - *(ii) for* $\mathcal{R}_+ \neq \varnothing$, E_* *is asymptotically stable for* $R \in \mathcal{R}_+$ *and unstable for* $R \in \mathcal{R}_-$, *and system* (1.1) *undergoes Turing bifurcation for* $R \in \mathcal{R}_0$.

Biological interpretation 1:

(1-1) Consider the case $\tau = 0$, which implies that the parasitism time is neglected and the prey dies immediately after being parasitized. When the perception intensity η is low, regardless of the perception scale R, only regions with sufficiently high density of *Monochamus saltuarius* can attract a significant number of natural enemies. After the parasitoid wasp *Sclerodermus guani* aggregates, it rapidly suppresses the beetle population to a low level, thereby achieving effective pest control. This behavior is consistent with the theoretical conclusion of local asymptotic stability.

(1-2) When the perception intensity satisfies $\eta > \eta^{(1)}$, the searching ability of *Sclerodermus guani* is markedly enhanced. In this regime, the size of the perception range R dictates the spatial dynamics of the system. If $R < R^{-}$, the natural enemy's perception is highly localized. Although it can quickly suppress high-density beetle patches, it is insufficient to induce large-scale population oscillations. If $R > R^{+}$, the natural enemy can perceive the beetle distribution almost globally, thereby avoiding excessive local aggregation and the subsequent population collapse, and instead maintains a spatially balanced regulation.

(1-3) When $R^{-} < R < R^{+}$, the perception range of the natural enemy lies in an intermediate state—it is attracted even to regions with medium or low beetle density, yet it cannot effectively avoid the risk of local resource depletion. This leads to a cyclic spatial pattern: Natural enemies aggregate in a low-density patch, deplete the beetles, and then themselves collapse due to the lack of hosts. Meanwhile, beetles in more distant regions recover quickly through diffusion and reproduction. Such spatially out-of-phase growth and decay corresponds to the occurrence of a Turing bifurcation in the theoretical analysis, resulting in the emergence of regular spatial patterns in the system.

2.2. Hopf bifurcation

In this section, we investigate the existence of Hopf bifurcation near the positive steady state E_* of system (1.1). By Theorem 2.3, we know that when $\tau = 0$ and $\eta \in (0, \eta^{(1)})$, the positive steady state E_* is locally asymptotically stable. Here, we choose a fixed value $\eta_* \in (0, \eta^{(1)})$, and for the sake of simplicity, we still denote η_* by η. Let $\tau > 0$, substitute $\lambda = \pm i\omega_n$ ($\omega_n > 0$, $n \in \mathbb{N}$) into Eq (2.1), and separate the real and imaginary parts; we obtain

$$\begin{cases} \cos(\omega_n \tau) = \dfrac{\omega_n^2 - G_n}{C}, \\ \sin(\omega_n \tau) = \dfrac{P_n \omega_n}{C} > 0, \end{cases} \tag{2.4}$$

where

$$\begin{cases} P_n = (d_1 + d_2)\left(\dfrac{n\pi}{L}\right)^2 - a_{11}, \\ G_n = d_1 d_2 \left(\dfrac{n\pi}{L}\right)^4 - d_2 a_{11} \left(\dfrac{n\pi}{L}\right)^2 - a_{21} a_{12} - a_{12} \eta v_* \left(\dfrac{n\pi}{L}\right)^2 \dfrac{\sin\left(\dfrac{n\pi R}{L}\right)}{\dfrac{n\pi R}{L}}, \\ C = -a_{12} b_{21}. \end{cases}$$

By squaring both the real and imaginary parts and adding them together, we obtain:

$$\omega_n^4 + \left(P_n^2 - 2G_n\right)\omega_n^2 + G_n^2 - C^2 = 0. \tag{2.5}$$

According to Eq (2.1) and assumption (H_2), we have $a_{11} < 0$, $a_{12} < 0$, $a_{21} > 0$, and $b_{21} > 0$, from which it is obvious that $C > 0$. For P_n, we get $(d_1 + d_2)(\frac{n\pi}{L})^2 - a_{11} \geq -a_{11} > 0$. For G_n, we can only guarantee that $G_0 = -a_{12} a_{21} > 0$.

Let $z_n = {\omega_n}^2$, we have $\mathscr{T}(z_n) \triangleq z_n^2 + \left(P_n^2 - 2G_n\right) z_n + G_n^2 - C^2$. The discriminant is given by $\Delta_2 = \left(P_n^2 - 2G_n\right)^2 - 4\left(G_n^2 - C^2\right) = P_n^4 - 4P_n^2 G_n + 4C^2$. We define the following sets:

$$\mathbb{P}_1 \triangleq \left\{ n \mid G_n^2 - C^2 \geq 0,\ P_n^2 - 2G_n \geq 0 \text{ and } P_n^4 - 4P_n^2 G_n + 4C^2 < 0,\ P_n^2 - 2G_n < 0,\ n \in \mathbb{N} \right\},$$
$$\mathbb{P}_2 \triangleq \left\{ n \mid G_n^2 - C^2 > 0,\ P_n^2 - 2G_n < 0 \text{ and } P_n^4 - 4P_n^2 G_n + 4C^2 > 0,\ n \in \mathbb{N} \right\},$$
$$\mathbb{P}_3 \triangleq \left\{ n \mid G_n^2 - C^2 < 0,\ n \in \mathbb{N} \right\},$$
$$\mathbb{P}_4 \triangleq \left\{ n \mid G_n^2 - C^2 = 0 \text{ and } P_n^2 - 2G_n < 0,\ n \in \mathbb{N} \right\}.$$

Therefore, we have the following lemma.

Lemma 2.2. *For the characteristic equation* (2.1)*, the following conclusions hold:*

1) *If $n \in \mathbb{P}_1$, then Eq* (2.1) *has no purely imaginary roots for any time delay $\tau > 0$;*

2) *If $n \in \mathbb{P}_2$, then there exist critical delays*

$$\tau_{n,j}^{\pm} = \frac{\arccos\left(\frac{(\omega_n^{\pm})^2 - G_n}{C}\right) + 2j\pi}{\omega_n^{\pm}}, \quad j \in \mathbb{N}_0,$$

such that Eq (2.1) *has two pairs of purely imaginary roots $\pm i\omega_n^{\pm}$ when $\tau = \tau_{n,j}^{\pm}$. Here, $\omega_n^{\pm}$ are the two positive roots of Eq* (2.5)*, satisfying*

$$\omega_n^{\pm} = \sqrt{\frac{1}{2}\left(2G_n - P_n^2 \pm \sqrt{P_n^4 - 4P_n^2 G_n + 4C^2}\right)}.$$

3) *If $n \in \mathbb{P}_3 \cup \mathbb{P}_4$, then there exists a critical delay*

$$\tau_{n,j}^{+} = \frac{\arccos\left(\frac{(\omega_n^{+})^2 - G_n}{C}\right) + 2j\pi}{\omega_n^{+}}, \quad j \in \mathbb{N}_0,$$

such that Eq (2.1) *has a unique pair of purely imaginary roots $\pm i\omega_n^{+}$ when $\tau = \tau_{n,j}^{+}$. Here, ω_n^{+} is the unique positive root of Eq* (2.5)*, satisfying*

$$\omega_n^{+} = \sqrt{\frac{1}{2}\left(2G_n - P_n^2 + \sqrt{P_n^4 - 4P_n^2 G_n + 4C^2}\right)}.$$

Lemma 2.3. *For the characteristic equation* (2.1)*, the transversality conditions are satisfied as follows.*

1) *For $n \in \mathbb{P}_2$, the real part of the derivative satisfies*

$$\operatorname{Re}\left(\frac{\mathrm{d}\lambda}{\mathrm{d}\tau}\right)\Bigg|_{\tau=\tau_{n,j}^{+}} = \frac{\sqrt{P_n^4 - 4P_n^2 G_n + 4C^2}}{C^2} > 0,$$

$$\operatorname{Re}\left(\frac{\mathrm{d}\lambda}{\mathrm{d}\tau}\right)\Bigg|_{\tau=\tau_{n,j}^{-}} = \frac{-\sqrt{P_n^4 - 4P_n^2 G_n + 4C^2}}{C^2} < 0,$$

for all $j \in \mathbb{N}_0$.

2) *For $n \in \mathbb{P}_3 \cup \mathbb{P}_4$, we have*

$$\mathrm{Re}\left(\frac{\mathrm{d}\lambda}{\mathrm{d}\tau}\right)\Bigg|_{\tau=\tau^{+}_{n,j}} = \frac{\sqrt{P_n^4 - 4P_n^2 G_n + 4C^2}}{C^2} > 0,$$

for all $j \in \mathbb{N}_0$.

Based on the above lemmas, we present the following theorem.

Theorem 2.4. *Suppose that assumptions (H_1) and (H_2) hold. For $0 \leq \eta < \eta^{(1)}$, the stability of the positive steady state E_* of system (1.1) with respect to the time delay τ satisfies the following conclusions.*

1) *If $n \in \mathbb{P}_1$, then the positive steady state E_* of system (1.1) is locally asymptotically stable for any $\tau \geq 0$.*
2) *If $n \in \mathbb{P}_2 \cup \mathbb{P}_3 \cup \mathbb{P}_4$, let*

$$\tau_c = \min\left\{\tau^{\pm}_{0,0}, \min_{n\in\mathbb{P}_2\cup\mathbb{P}_3\cup\mathbb{P}_4} \tau^{\pm}_{n,0}\right\},$$

and thus we have the two following results.

   - (a) *When $\tau \in [0, \tau_c)$, the positive steady state E_* of system (1.1) is locally asymptotically stable;*
   - (b) *When $\tau > \tau_c$, the positive steady state E_* of system (1.1) either remains unstable or undergoes stability switches as τ further increases. Moreover, system (1.1) undergoes a n_0-mode Hopf bifurcation at the positive steady state E_* when $\tau = \tau^{\pm}_{n_0,j}$ ($n_0 \in \mathbb{P}_2 \cup \mathbb{P}_3 \cup \mathbb{P}_4$, $j \in \mathbb{N}_0$).*

Biological interpretation 2: Considering the time delay $\tau > 0$, the stability of the system changes significantly. When τ is small, the delay effect is weak, and the system remains locally asymptotically stable around the positive equilibrium point. As τ increases and crosses the critical value τ_c, the delay effect is enhanced. After parasitizing the host, *Sclerodermus guani* needs to undergo a certain period of time to complete nutrient absorption and individual development until the emergence and proliferation of new adult wasps. The time delay in this developmental process prevents the natural enemy population from promptly responding in regulating the host population, ultimately leading to a significant lagged feedback effect. This feedback delay causes the system to lose stability and generate periodic temporal oscillations—that is, the population sizes of *Monochamus saltuarius* and its natural enemies exhibit regular periodic fluctuations over time instead of maintaining a steady state. This dynamical behavior corresponds to the periodic population fluctuations commonly observed in biological control practices.

2.3. Turing-Hopf bifurcation

In this section, we investigate the Turing-Hopf bifurcation of system (1.1). Based on the separate analysis of the Turing bifurcation and the Hopf bifurcation in the preceding sections, we derive the following theorem concerning the existence of the Turing-Hopf bifurcation.

Theorem 2.5. *Suppose assumptions (H_1) and (H_2) hold and $n \in \mathbb{P}_2 \cup \mathbb{P}_3 \cup \mathbb{P}_4$, then we have the following conclusions:*

1) *If* $\eta = \eta^{(1)}$*, system* (1.1) *undergoes a Turing–Hopf bifurcation at* $(R, \tau) = (R_0^*, \tau_c)$*;*

2) *If* $\eta > \eta^{(1)}$*, system* (1.1) *undergoes a Turing–Hopf bifurcation at* $(R, \tau) = (R^-, \tau_c)$ *or* $(R, \tau) = (R^+, \tau_c)$*.*

Biological interpretation 3: When $\eta > \eta^{(1)}$, *Sclerodermus guani* can sufficiently detect patches of *Monochamus saltuarius* with medium-to-low density. If the perception range satisfies $R^- < R < R^+$, natural enemies will be attracted to these medium-to-low density beetle patches, resulting in local over-predation and subsequent collapse of the natural enemy population. At this time, if the parasitic time delay $\tau > \tau_c$, it means that *Sclerodermus guani* requires a certain period to complete nutrient absorption, individual development, and emergence of new adults after parasitizing *Monochamus saltuarius*, which induces a lag in the regulatory effect of natural enemies and disrupts the temporal balance of the system. These two mechanisms act synergistically, leading to a complex dynamical phenomenon where the population dynamics of *Monochamus saltuarius* and its natural enemies form non-uniform spatial patterns in the spatial dimension and undergo periodic oscillations in the temporal dimension simultaneously.

3. Numerical simulations

In this section, we first determine biologically realistic parameter values by referencing relevant published literature. We then substitute these parameters into the model to perform numerical simulations for the Turing bifurcation, Hopf bifurcation, and Turing-Hopf bifurcation derived in the theoretical analysis. The simulation results are used to verify the correctness of our theoretical derivation and intuitively characterize the rich spatiotemporal dynamic behaviors of the system under different parameter conditions.

3.1. Selection of parameter values

It should be pointed out that in ecological research, the measurement of some mathematical parameters faces considerable difficulties, such as the population carrying capacity and diffusion coefficient. In addition, different geographical locations, climatic conditions, tree species, and even different biotypes of parasitoid wasps correspond to different parameter values in mathematical models. To select parameters as scientifically as possible and better serve practical applications, we adopt the following strategy. For parameters with well-documented values, we directly adopt those reported values. For ecologically difficult-to-measure parameters, we reasonably estimate them based on literature surveys and statistical methods. For a small number of highly uncertain parameters, we assign values within reasonable ranges.

1) Intrinsic growth rate of *Monochamus saltuarius*: r

Due to the lack of available data on the intrinsic growth rate of *Monochamus saltuarius*, the relevant parameters of its congener *Monochamus alternatus* are used as a substitute in our study. As shown in Figure 3, Wen et al. [22] systematically monitored the flight seasonal dynamics of adult *Monochamus alternatus* in experimental pine forests in Xingan County, Jiangxi Province, China from 2016 to 2017 by hanging traps.

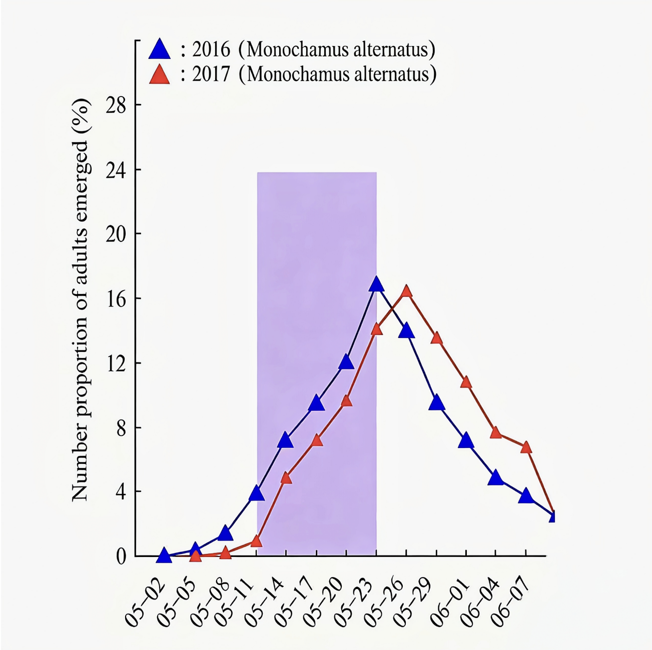

Figure 3. Emergence dynamics of *Monochamus alternatus* adults.

A conservative estimation approach has been adopted in this study: The growth rate of the eclosing adult longhorn beetle proportion is approximately regarded as the intrinsic growth rate r, with the calculation formula as follows:

$$\text{Growth rate of eclosing adult proportion} = \frac{\text{Change in eclosing adult proportion}}{\text{Initial value of eclosing adult proportion}}.$$

The unit of time is one week. We select representative data from May 11–23, the light purple region in Figure 3, and obtain that the growth rate of the eclosing adult proportion ranges from 0.35 to 0.7. For conservatism, we choose $r = 0.4$ as the intrinsic growth rate.

2) Predation efficiency: γ and handling time: h

In terms of predation behavior, *Sclerodermus guani* is similar to *Sclerodermus alternatus*. According to Yang et al. [19], we refer to the predation rate and handling time of *Sclerodermus alternatus*. The instantaneous attack rate of predation is 0.1277 per day and $h = 0.66$ days. Since the unit time in our study is chosen as one week, we have $\gamma = 0.9$ and $h = 0.09$.

3) Parasitism efficiency: α

According to Yang et al. [19], the instantaneous attack rate of *Sclerodermus alternatusi* on *Monochamus alternatus* is 0.0294. However, referring to Zheng et al. [20], *Sclerodermus guani* exhibits a higher parasitism rate when parasitizing *Monochamus saltuarius*. Based on this, we reasonably assume the instantaneous attack rate to be 0.4, which yields $\alpha = 0.28$.

4) Other parameters: d_1, d_2, K, ξ, d_3, δ and β

According to Jung et al. [23], we reasonably select the diffusion coefficient of *Monochamus saltuarius* as $d_1 = 0.002$. Since *Sclerodermus guani* searches for *Monochamus saltuarius* through chemical cues, its diffusion capacity can be considered stronger, and thus we set $d_2 = 0.003$. For the remaining parameters, the following values are adopted: $K = 2$, $\delta = 0.3$, $\beta = 0.3$, $\xi = 0.1$, and $d_3 = 0.03$.

In summary, the parameters listed in Table 1 are selected for numerical simulation.

Table 1. Parameter values and references.

Parameter	Value	Unit	Reference
d_1	0.002	$km^2 week^{-1}$	Jung et al. [23]
d_2	0.003	$km^2 week^{-1}$	–
d_3	0.03	$week^{-1}$	–
r	0.4	$week^{-1}$	Wen et al. [22]
K	2	$\times 10^4 (km^2)^{-1}$	–
α	0.28	$week^{-1}$	Yang et al. [19] & Zheng et al. [20]
γ	0.9	$week^{-1}$	Yang et al. [19]
h	0.09	$week$	Yang et al. [19]
ξ	0.1	-	–
δ	0.3	-	–
β	0.3	-	–

3.2. *Phenomena of numerical simulation*

Under the above parameters, (H_1) holds. Then, system (1.1) has the positive constant steady state $E_* = (u_*, v_*) = (0.085191, 0.241058)$. It can be easily verified that assumption (H_2) holds. Without loss of generality, we choose $L = 6$ and give the following initial function:

$$u_0(x,t) = 0.085191 + 0.01\cos(x),\ v_0(x,t) = 0.241058 + 0.01\cos(x),\ x \in [-L, L]. \tag{3.1}$$

In this case, according to Theorem 2.2, the system (1.1) is locally asymptotically stable when $\tau = 0$ and $\eta = 0$, as illustrated in Figure 4.

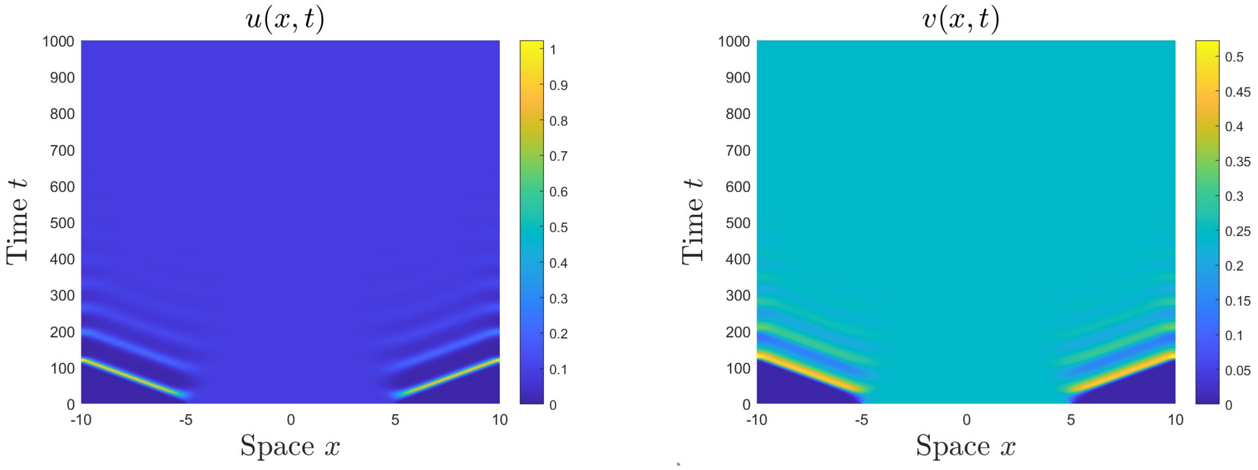

(a) **(b)**

Figure 4. Simulated solution near the positive steady state E_*: The positive constant steady state E_* for system (1.1) is locally asymptotically stable when $\tau = 0$ and $\eta = 0$.

3.2.1. Turing bifurcation induced by the perception range R and the perception diffusion intensity η

Since $j \in \{2m-1 \mid m \in \mathbb{N}\}$, the first three positive solutions of $\tan z_j = z_j$ are $z_1 = 4.4934$, $z_2 = 10.9041$, and $z_3 = 17.2208$. Then, by Lemma 2.1, we have

$$\eta^{(1)} = 0.094885;\ \eta^{(2)} = 0.225701;\ \eta^{(3)} = 0.355555.$$

We first investigate the variations of R^- and R^+ with η under the condition $\eta^{(1)} < \eta < \eta^{(2)}$, as shown in Figure 5. We select $\eta = 0.15$, and the corresponding island region is shown in Figure 6.

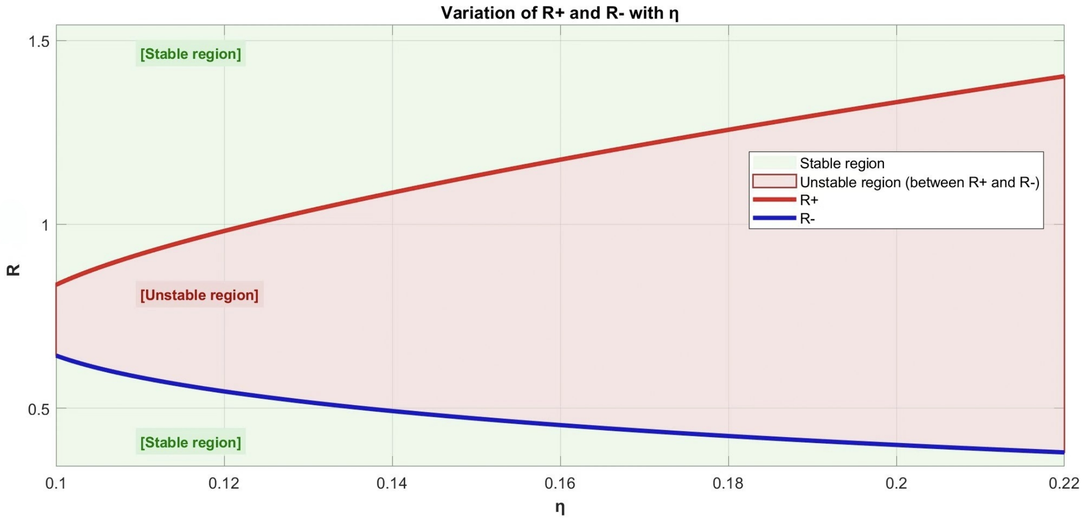

Figure 5. Variation of R^+ and R^- with η: When $\eta \in (\eta^{(1)}, \eta^{(2)})$, the Turing bifurcation threshold R^- decreases with the increase of η, while R^+ increases as η rises.

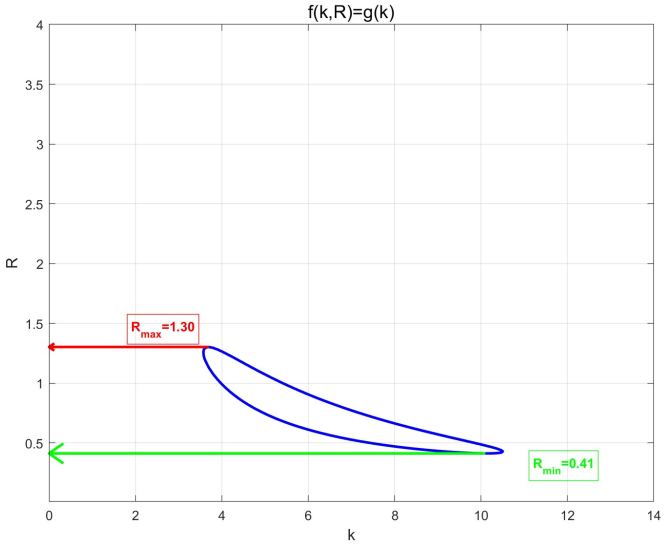

Figure 6. Island-like region for $\eta = 0.15$: The island-like region enclosed by $f(k, R) = g(k)$ is presented. From the figure, it can be readily derived that $k_2 = 1.94$, $R^+ = 1.3$; $k_1 = 5.28$, $R^- = 0.41$.

According to Theorem 2.3, when $\eta = 0.09 < \eta^{(1)}$, the positive constant steady state E_* of system (1.1) is locally asymptotically stable; see Figure 7. This corresponds to the biological interpretation given in (1-1). Let $\eta = 0.15$: When $R = 0.38 < R^-$, E_* remains locally asymptotically stable, which corresponds to biological interpretations (1-2); see Figure 8. When $R = 0.48 \in (R^-, R^+)$, the system exhibits nonhomogeneous steady-state solutions, which corresponds to biological interpretations (1-3) and the striped region in Figure 2(b); see Figure 9. When $R = 1.5 > R^+$, the positive equilibrium E_* is locally asymptotically stable, which corresponds to biological interpretations (1-2); see Figure 10. In summary, we present the schematic diagram of the Turing unstable region, with the above simulation points marked in Figure 11.

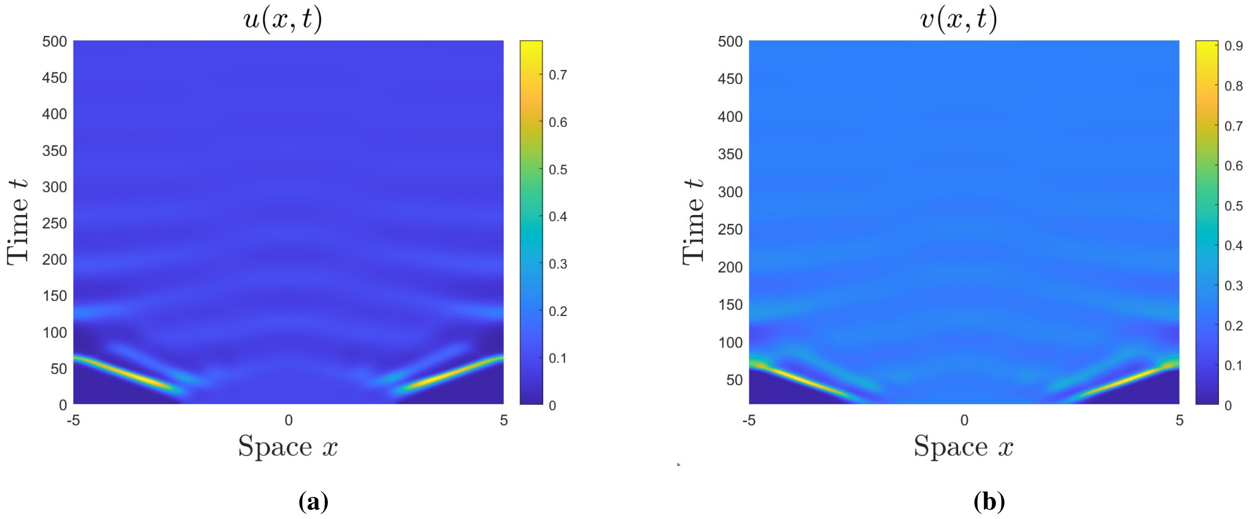

(a) **(b)**

Figure 7. Simulated solution near the positive steady state E_*: For the point $A : (\eta, R) = (0.09, 1.0)$, the positive steady state E_* of system (1.1) is locally asymptotically stable.

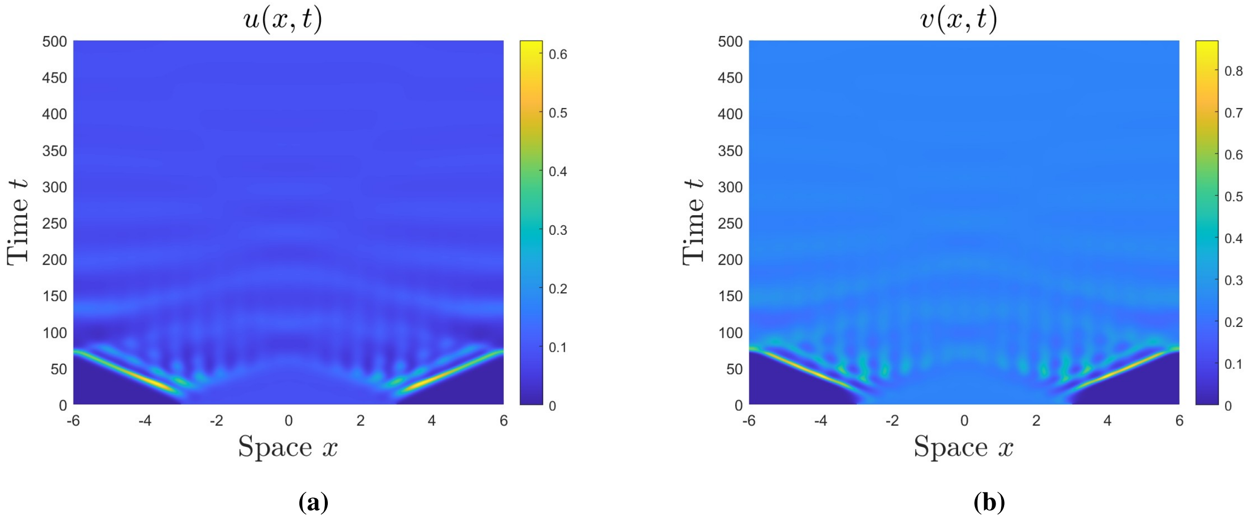

(a) **(b)**

Figure 8. Simulated solution near the positive steady state E_*: For the point $B : (\eta, R) = (0.15, 0.38)$, the positive steady state E_* of system (1.1) is locally asymptotically stable.

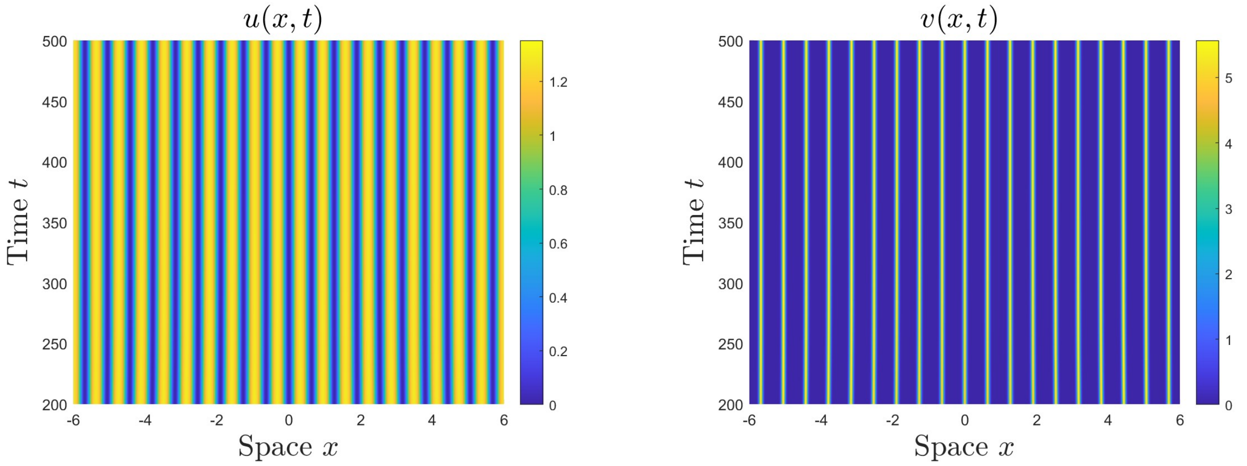

(a) **(b)**

Figure 9. Simulated solution near the positive steady state E_*: For the point C : $(\eta, R) = (0.15, 0.48)$, the positive steady state E_* of system (1.1) leads to the emergence of nonhomogeneous steady state solutions.

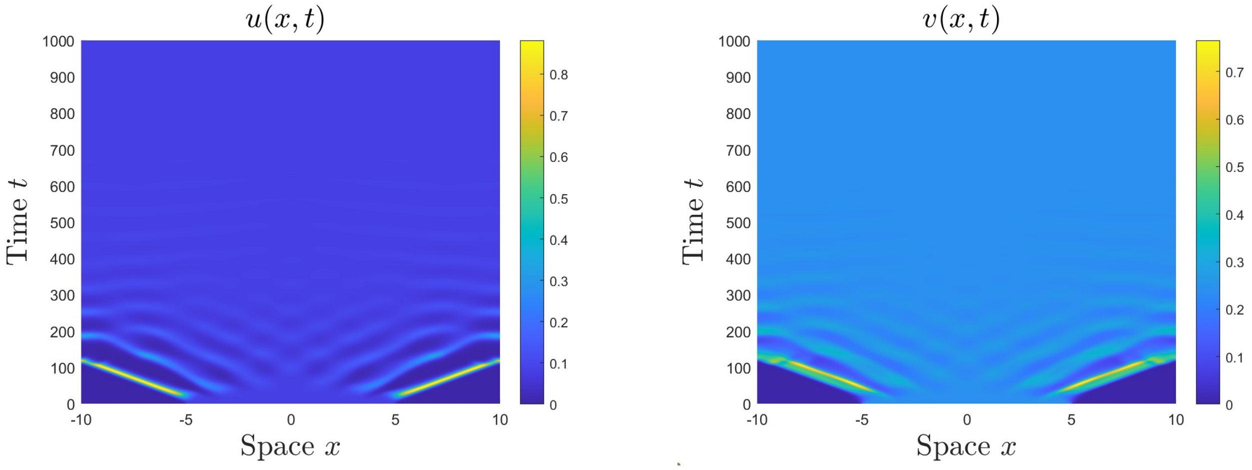

(a) **(b)**

Figure 10. Simulated solution near the positive steady state E_*: For the point D : $(\eta, R) = (0.15, 1.5)$, the positive steady state E_* of system (1.1) is locally asymptotically stable.

We first investigate the variations of R^- and R^+ with η under the condition $\eta^{(2)} < \eta < \eta^{(3)}$, as shown in Figure 12. We select $\eta = 0.32$, and the corresponding island region is shown in Figure 13. When $R = 2.38 \in (R^-, R^+)$, the positive equilibrium E_* gives rise to nonhomogeneous steady-state solutions; see Figure 14. When $R = 3.0 > R^+$, the positive equilibrium E_* is locally asymptotically stable; see Figure 15. In summary, we provide a schematic diagram of the Turing unstable region, with the above points marked in Figure 16.

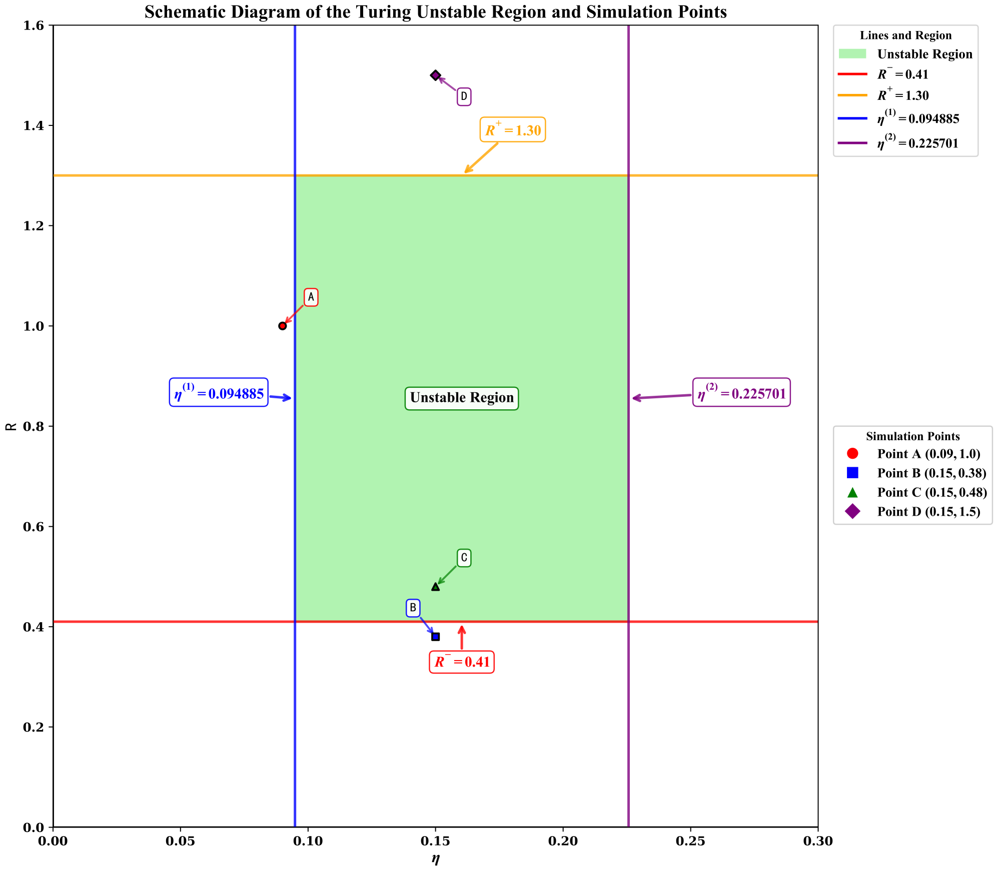

Figure 11. Schematic diagram of the Turing unstable region and simulation points.

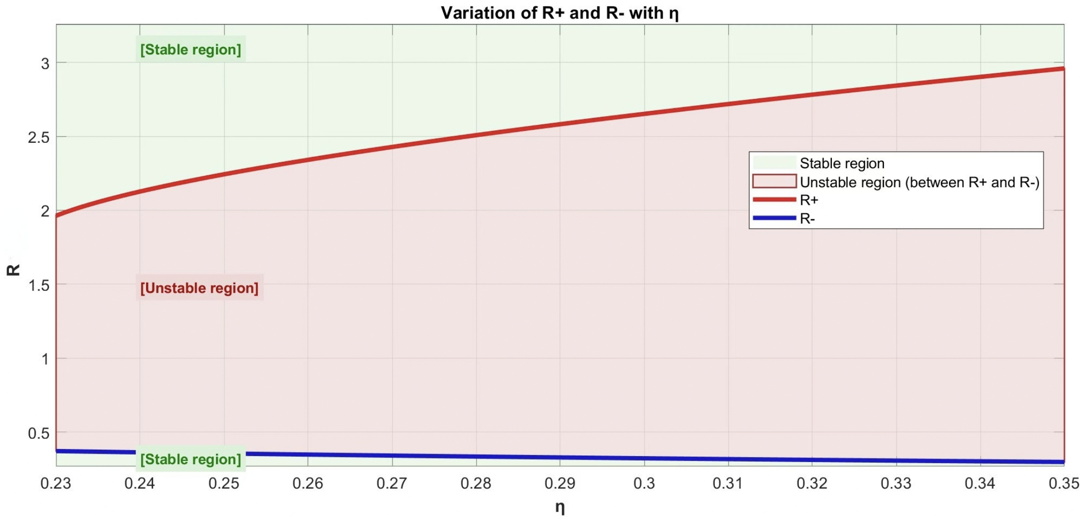

Figure 12. Variation of R^+ and R^- with η: When $\eta \in (\eta^{(2)}, \eta^{(3)})$, the Turing bifurcation threshold R^- decreases with the increase of η, while R^+ increases as η rises.

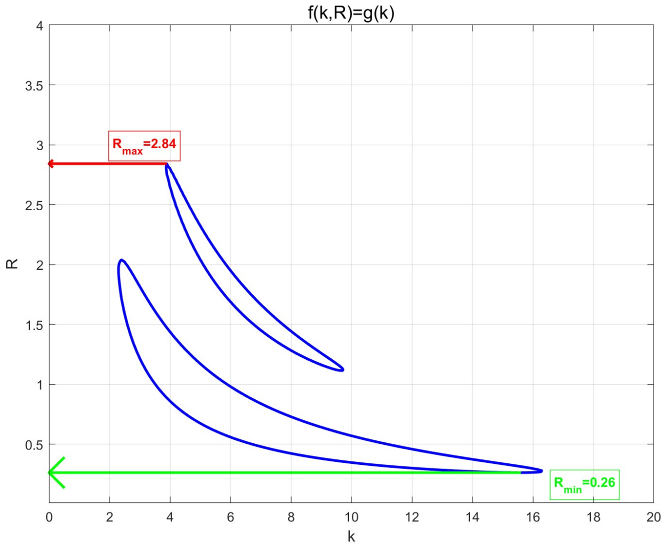

Figure 13. Island-like region for $\eta = 0.32$: The island-like region enclosed by $f(k, R) = g(k)$ is presented. From the figure, it can be readily derived that $k_2 = 3.90$, $R^+ = 2.84$; $k_1 = 15.60$, $R^- = 0.26$.

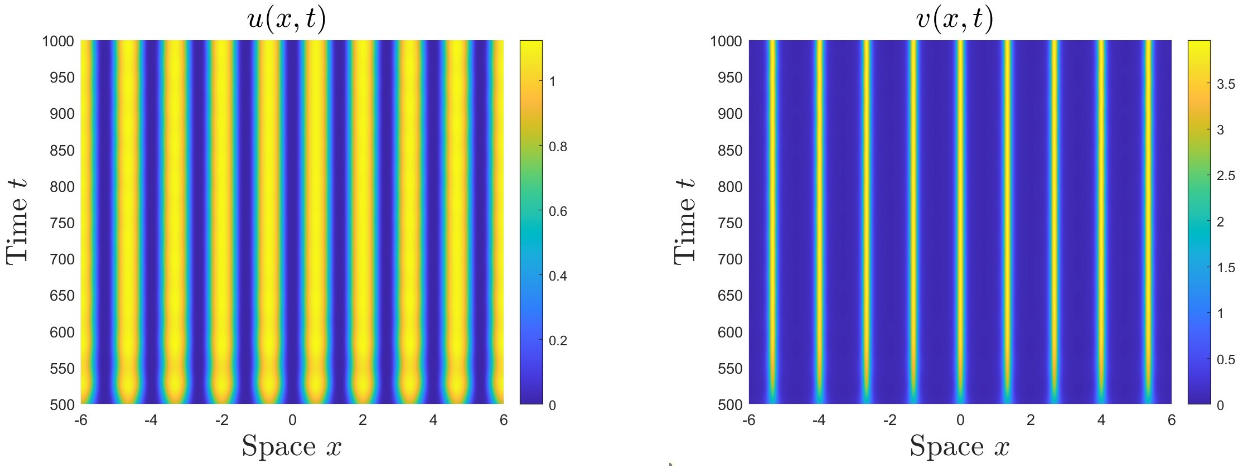

(a) **(b)**

Figure 14. Simulated solution near the positive steady state E_*: For the point $F : (\eta, R) = (0.32, 2.38)$, the positive steady state E_* of system (1.1) leads to the emergence of stable spatially nonhomogeneous solutions.

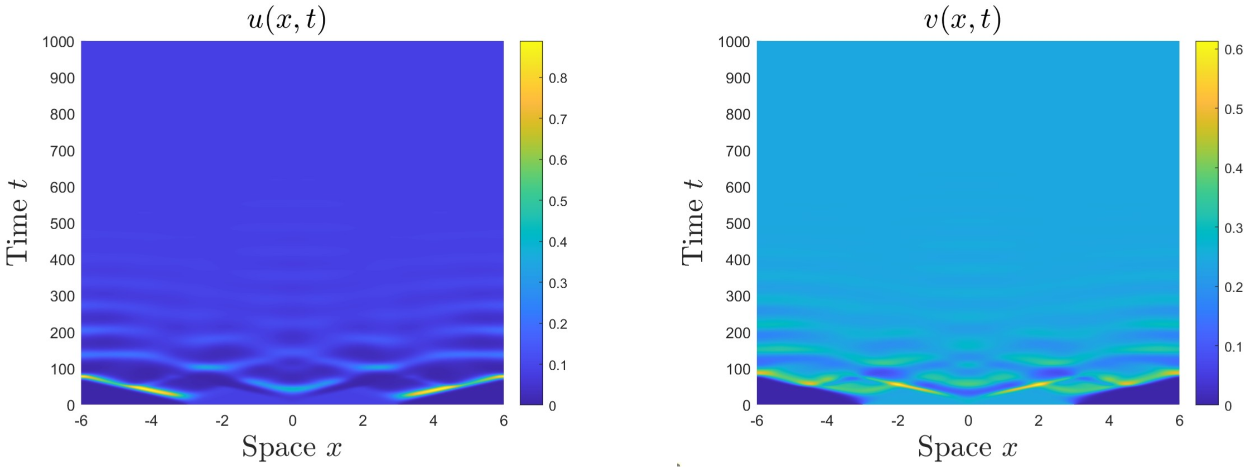

(a) **(b)**

Figure 15. Simulated solution near the positive steady state E_*: For the point $G : (\eta, R) = (0.32, 3.0)$, the positive steady state E_* of system (1.1) is locally asymptotically stable.

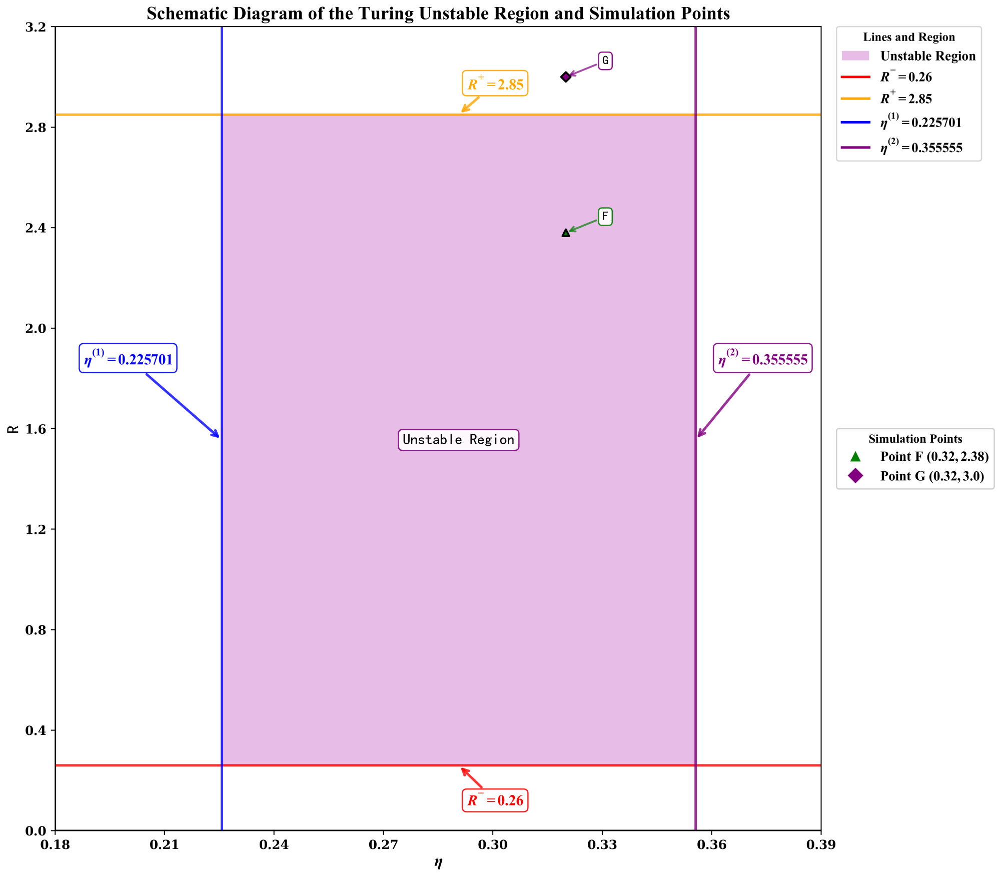

Figure 16. Schematic diagram of the Turing unstable region and simulation points.

3.2.2. Hopf bifurcation induced by the parasitic delay τ

Based on the above analysis, we fix $\eta = 0$ and $R = 1$, for which the critical value is $\tau_c = 8.35$. Next, we select $\tau = 3 < \tau_c$ and $\tau = 8.9 > \tau_c$ to verify the existence of the Hopf bifurcation, as shown in Figures 17 and 18.

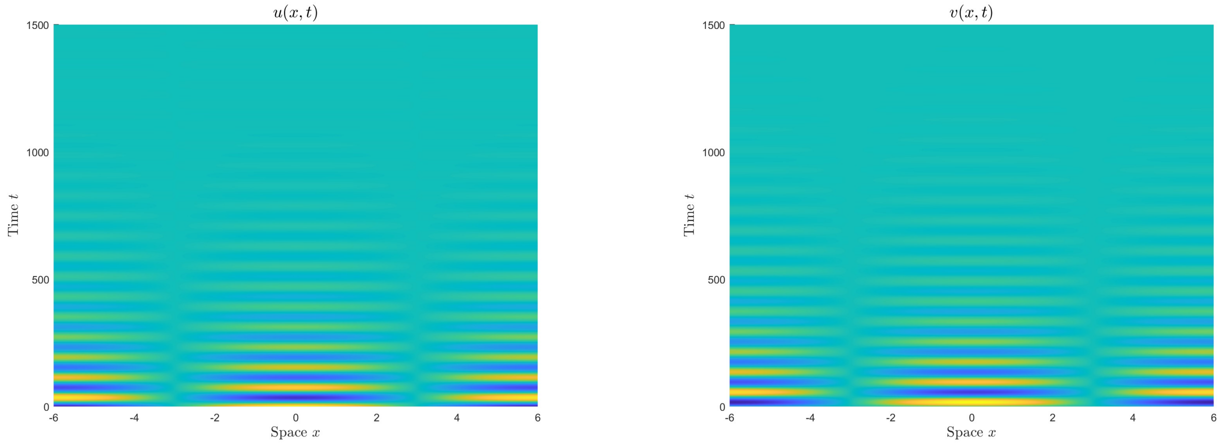

(a) **(b)**

Figure 17. Simulated solution near the positive steady state E_*: The positive steady state E_* of system (1.1) is locally asymptotically stable when $\tau = 3$.

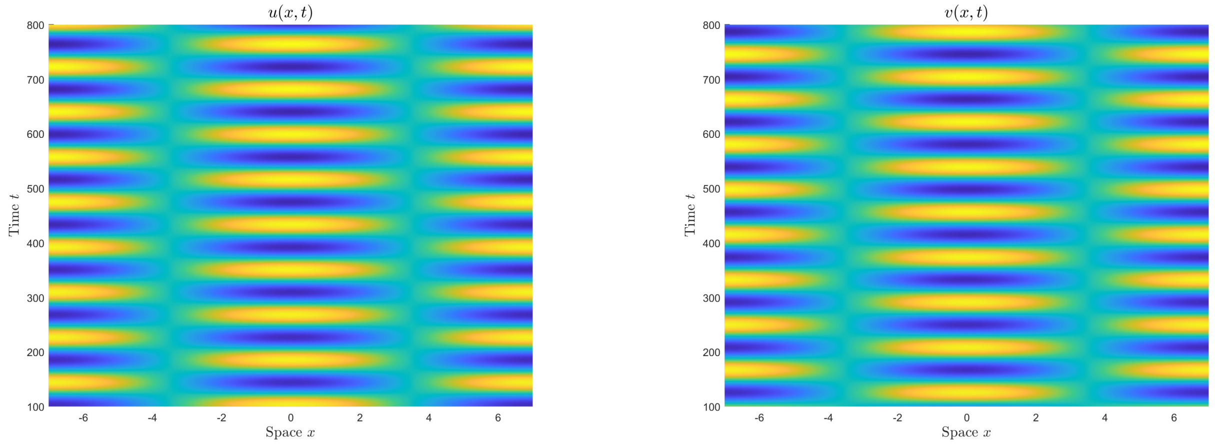

(a) **(b)**

Figure 18. Simulated solution near the positive steady state E_*: The positive steady state E_* of system (1.1) leads to the emergence of stable spatially nonhomogeneous periodic solutions when $\tau = 8.9$.

3.2.3. Turing-Hopf bifurcation induced by the perceptual scale R, the perceptual diffusion coefficient η, and the parasitic delay τ

According to Theorem 2.4, the critical delay τ_c is related to η and R. The relationship diagram among η, R, and τ_c is depicted in Figures 19 and 20. It can be observed that τ_c remains unchanged with the variation of η and R.

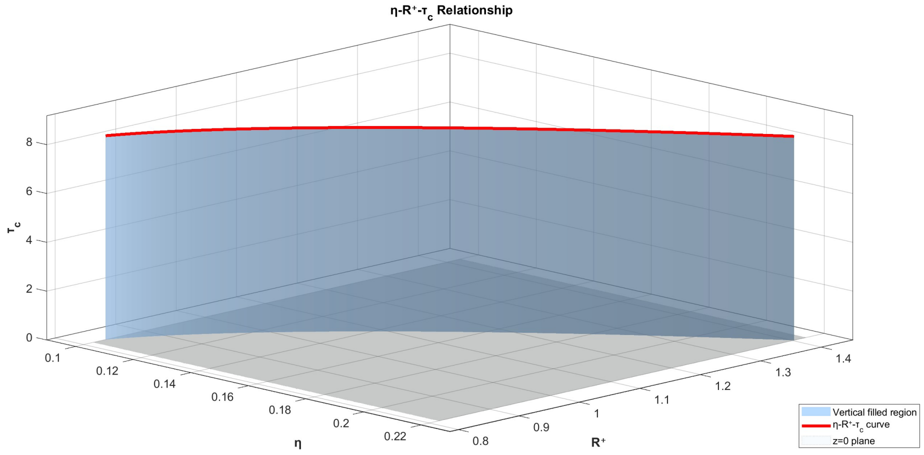

(a) $\eta - R^{+} - \tau_c$

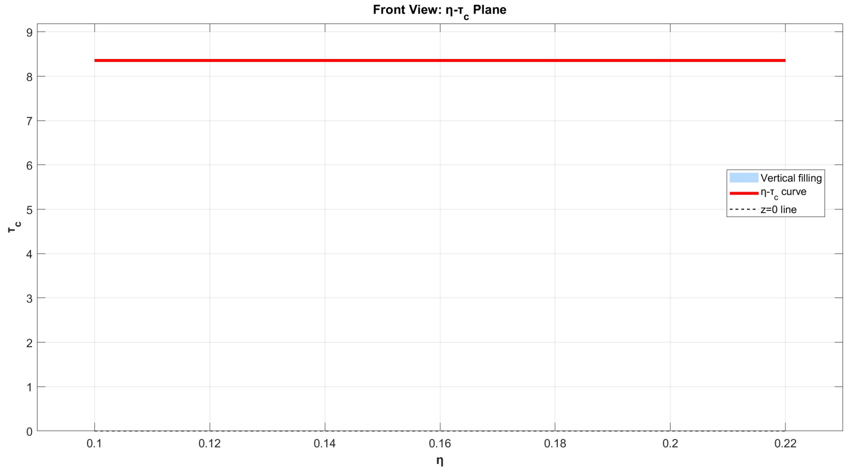

(b) $\eta - \tau_c$

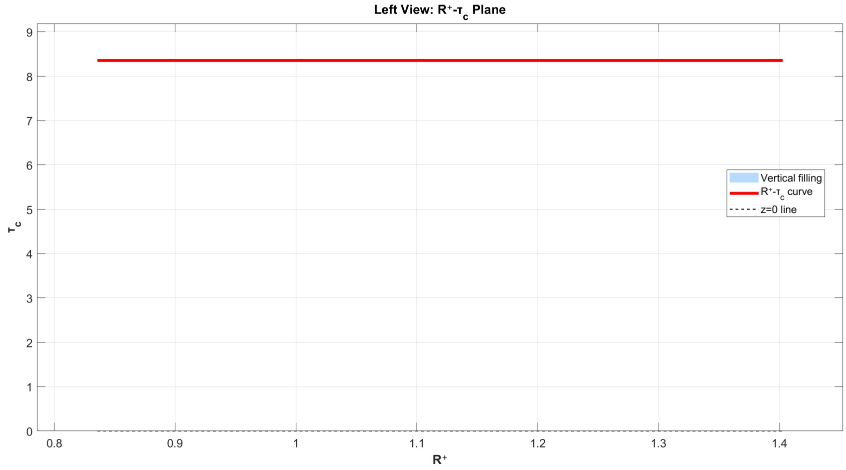

(c) $R^{+} - \tau_c$

Figure 19. 3D surface and cross-sectional plots of η-R^{+}-τ_c: For $\eta \in (\eta^{(1)}, \eta^{(2)})$, the critical value τ_c remains unchanged with the variation of R^{+} and η.

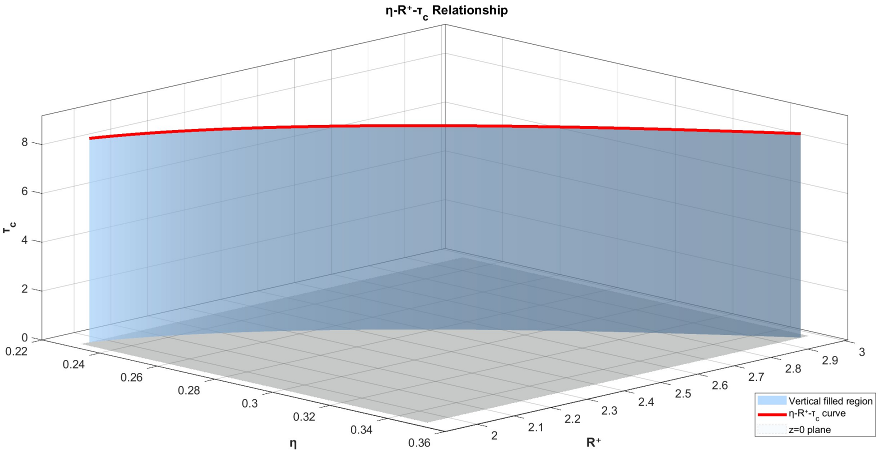

(a) $\eta - R^{+} - \tau_c$

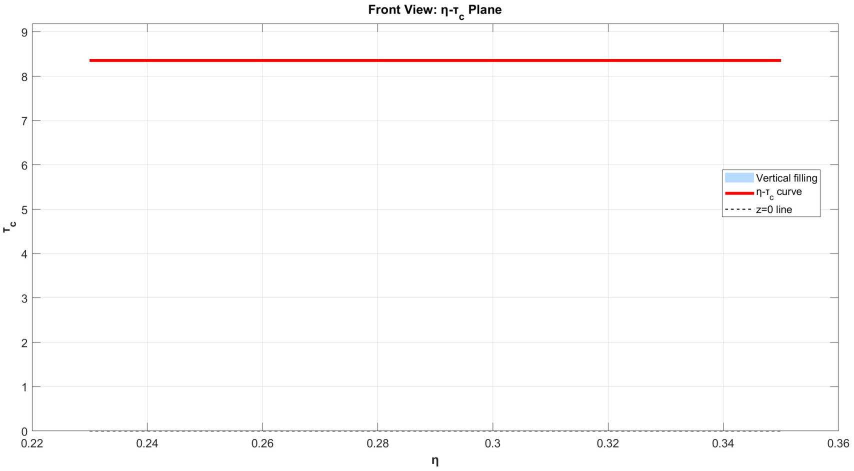

(b) $\eta - \tau_c$

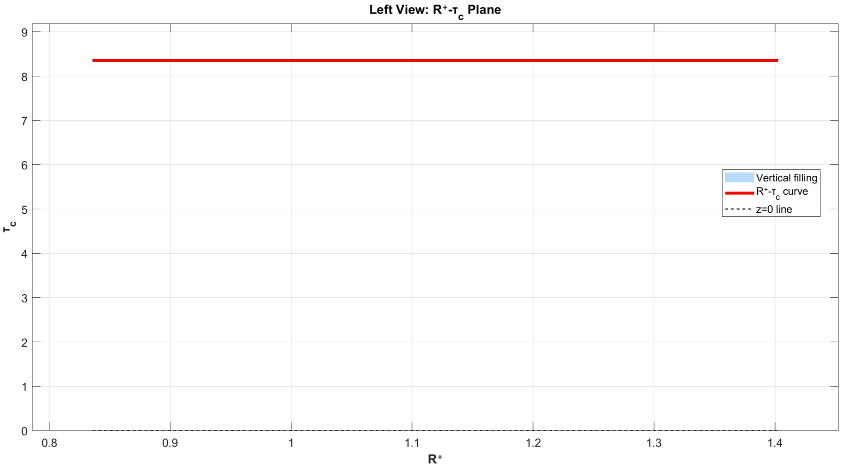

(c) $R^{+} - \tau_c$

Figure 20. 3D surface and cross-sectional plots of η-R^{+}-τ_c: For $\eta \in (\eta^{(2)}, \eta^{(3)})$, the critical value τ_c remains unchanged with the variation of R^{+} and η.

From Theorem 2.5, the positive constant steady state E_* of system (1.1) undergoes Turing-Hopf bifurcation at the point $(R, \tau) = (R^+, \tau_c)$. We choose $\eta = 0.15$, and from the previous analysis, we have $R^+ = 1.3$. The critical delay is calculated as $\tau_c = 8.35$, which is consistent with the information provided in Figure 19.

In the following, we select some points to simulate the dynamic behaviors. For the point $P : (R, \tau) = (1.3, 8.35)$, the positive constant steady state E_* of system (1.1) leads to the emergence of nonhomogeneous periodic solutions; see Figure 21. For the point $P_1 : (R, \tau) = (1.35, 8.4)$, the positive constant steady state E_* for system (1.1) leads to the emergence of nonhomogeneous periodic solutions; see Figure 22. For the point $P_2 : (R, \tau) = (1.2, 8.4)$, the positive constant steady state E_* for system (1.1) leads to the emergence of nonhomogeneous periodic solutions; see Figure 23. For the point $P_3 : (R, \tau) = (1, 8.2)$, the positive constant steady state E_* for system (1.1) leads to the emergence of nonhomogeneous steady-state solutions; see Figure 24. For the point $P_4 : (R, \tau) = (1.35, 8)$, the positive constant steady state E_* for system (1.1) is locally asymptotically stable; see Figure 25. In summary, we present a schematic diagram of the bifurcation region with the simulation points marked; see Figure 26.

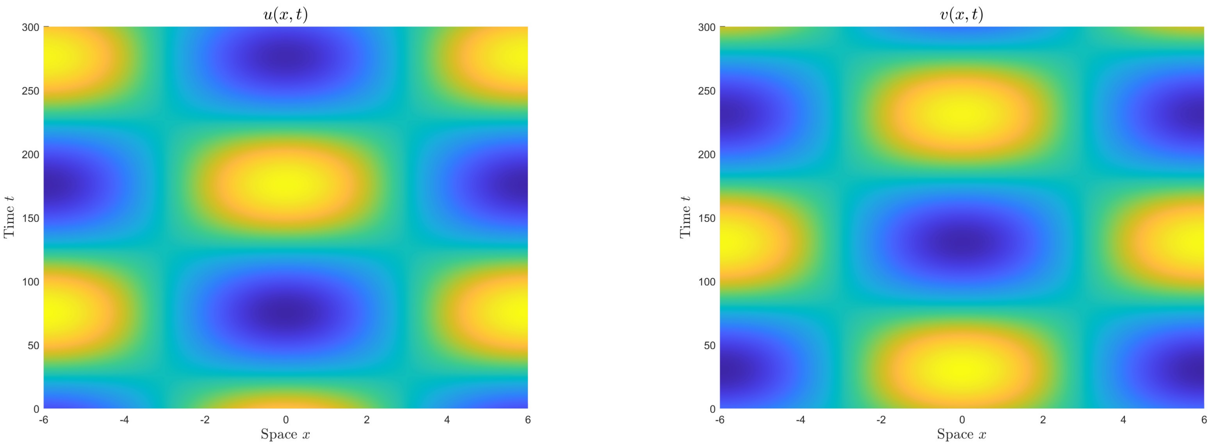

(a) **(b)**

Figure 21. Simulated solution near the positive steady state E_*: For the point $P : (R, \tau) = (1.3, 8.35)$, the positive steady state E_* of system (1.1) leads to the emergence of nonhomogeneous periodic solutions.

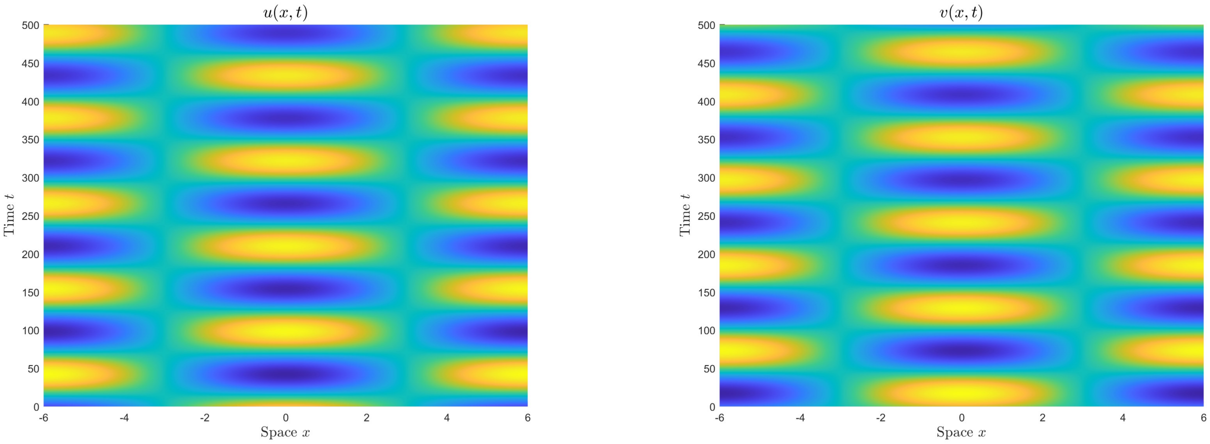

(a) **(b)**

Figure 22. Simulated solution near the positive steady state E_*: For the point P_1 : $(R, \tau) = (1.35, 8.4)$, the positive steady state E_* of system (1.1) leads to the emergence of nonhomogeneous periodic solutions.

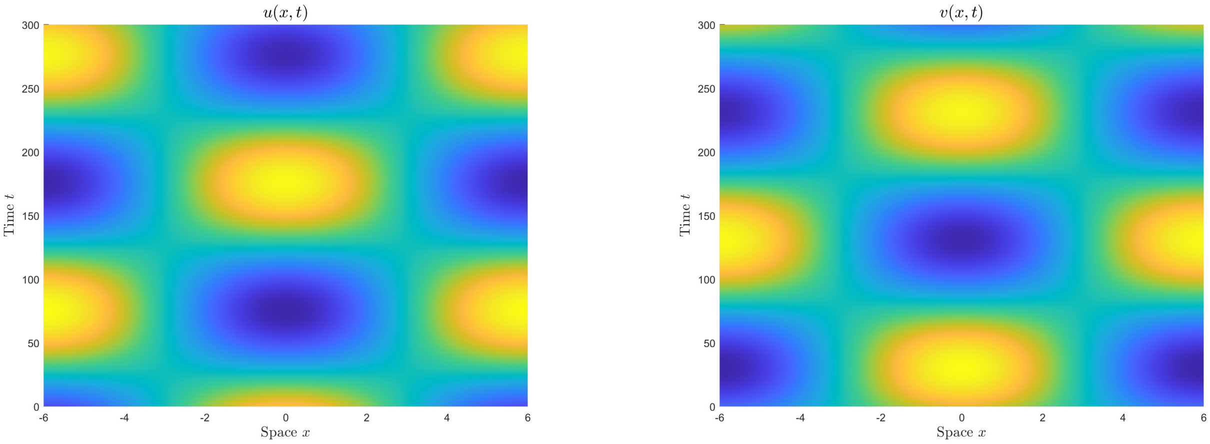

(a) **(b)**

Figure 23. Simulated solution near the positive steady state E_*: For the point P_1 : $(R, \tau) = (1.2, 8.4)$, the positive steady state E_* of system (1.1) leads to the emergence of nonhomogeneous periodic solutions.

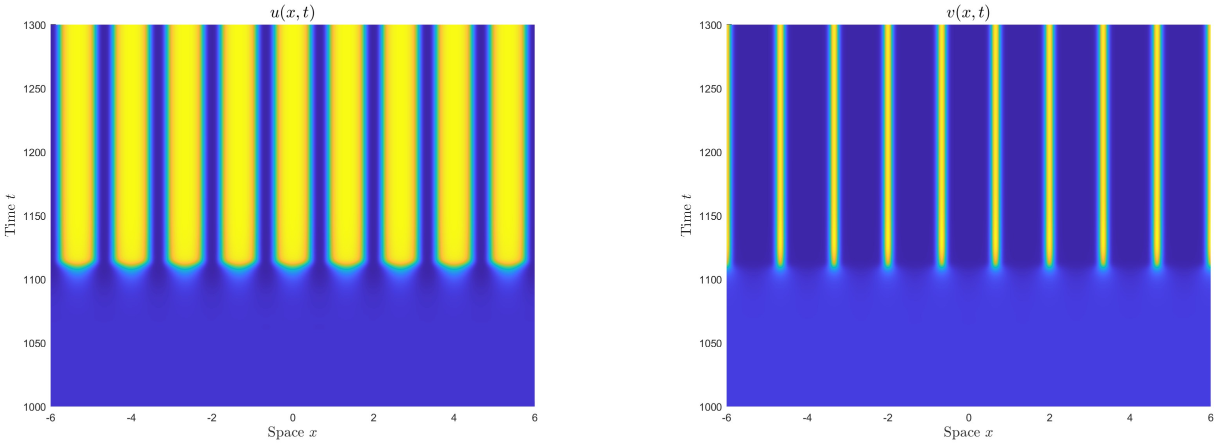

(a) **(b)**

Figure 24. Simulated solution near the positive steady state E_*: For the point P_3 : $(R, \tau) = (1, 8.2)$, the positive steady state E_* of system (1.1) leads to the emergence of nonhomogeneous steady-state solutions.

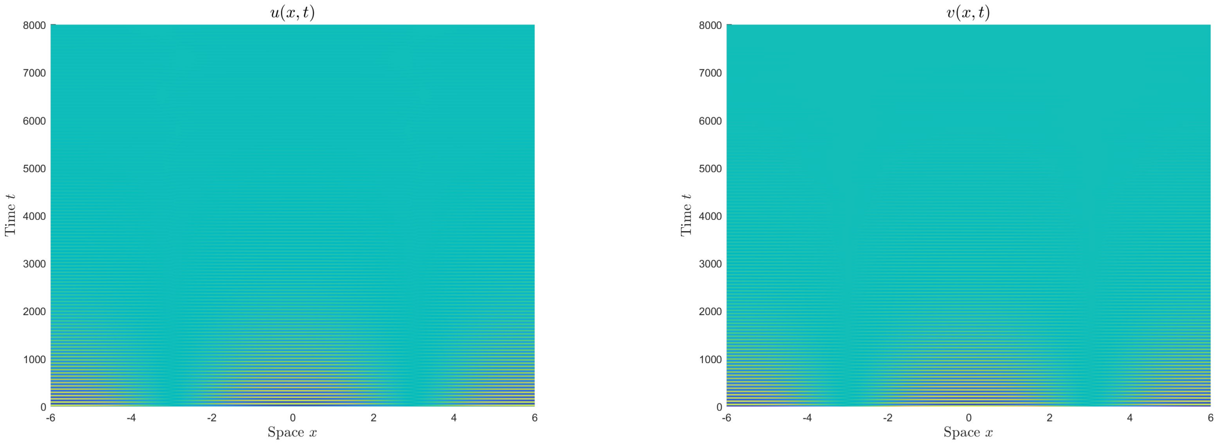

(a) **(b)**

Figure 25. Simulated solution near the positive steady state E_*: For the point P_4 : $(R, \tau) = (1.35, 8)$, the positive steady state E_* of system (1.1) is locally asymptotically stable.

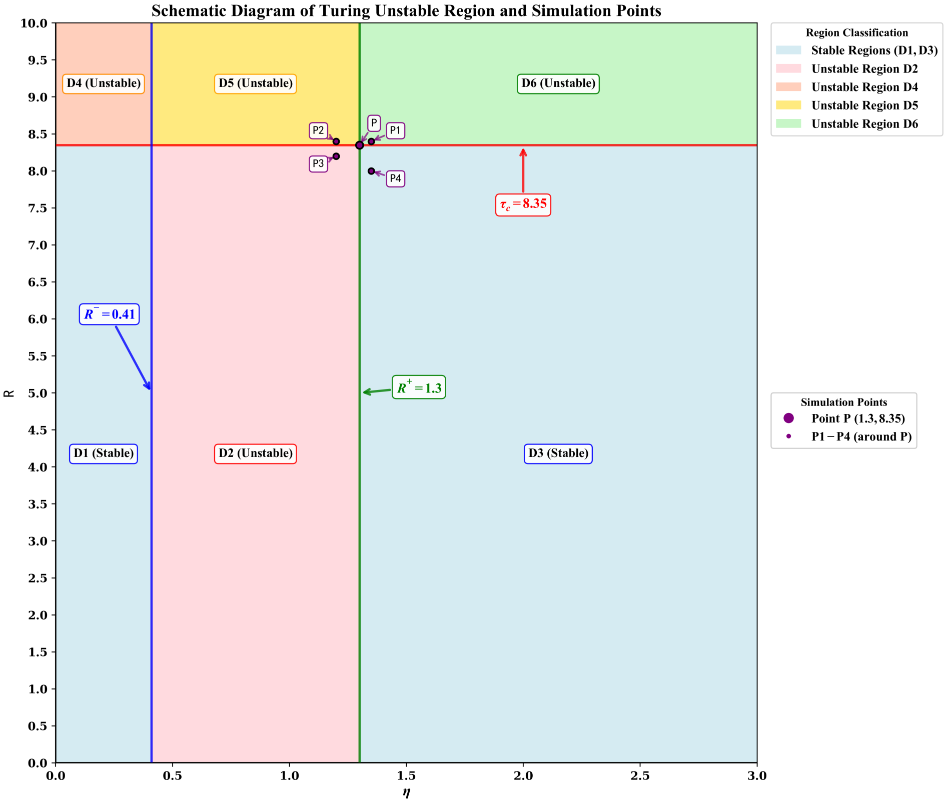

Figure 26. Schematic diagram of regional stability with simulation points.

3.3. *Recommendations for the control of Pine Wilt Disease*

Based on the above numerical simulations, we propose the following suggestions for the ecological practice of controlling *Monochamus saltuarius* using *Scleroderma guani*. Theoretical analysis and numerical simulations jointly show that the perception intensity η and perception range R of natural enemies are key parameters affecting spatially inhomogeneous solutions. When η exceeds the critical value $\eta^{(1)}$ and if the perception range R of natural enemies falls within the critical interval (R^-, R^+), the system will become unstable and may form harmful spatial aggregation patterns. Therefore, in the implementation of biological control, if the inherent perception ability of natural enemies is evaluated to be strong ($\eta > \eta^{(1)}$), artificial interference with their information acquisition should be carried out through stand thinning, physical barriers, or interval release, so as to control the effective perception range R below R^- or above R^+, thereby maintaining the system in a spatially uniform and stable state.

In the time dimension, the parasitic delay τ is a key parameter inducing Hopf bifurcation. When the delay τ exceeds the critical value τ_c, the predator-prey population will fall into sustained periodic oscillations, which greatly weakens the stability of control. Therefore, the release strategy must be highly synchronized with the life history of the host. It is recommended to release natural enemies timely during the early larval stage of *Monochamus saltuarius*, so as to minimize the time from parasitism to actual control effect and ensure $\tau < \tau_c$, thus avoiding harmful population fluctuations caused by time delay.

When $\eta > \eta^{(1)}$ and $\tau > \tau_c$, the system may undergo Turing-Hopf bifurcation, where the spatiotemporally coupled instability mode will make population dynamics extremely complex and unpredictable. This requires us to establish an early warning system integrating spatial distribution survey and temporal density monitoring. Through continuous estimation of key parameters η, τ, and R, we can predict whether the system state approaches the bifurcation threshold, so as to provide quantitative decision support for dynamically adjusting the release intensity, range, and timing.

In summary, combined with numerical simulations and theoretical analysis, by regulating the perception parameters η and R of the natural enemy *Scleroderma guani*, optimizing the release strategies related to the parasitic delay τ, and establishing a spatiotemporally coupled monitoring and early warning system, we can effectively avoid system instability and the formation of harmful spatial patterns, achieve precise and stable biological control of *Monochamus saltuarius*, and provide a reliable approach for the prevention and control of PWD.

4. Conclusions

Based on the biological background of controlling *Monochamus saltuarius* using *Sclerodermus guani*, this paper has established a reaction-diffusion equation model with dual functional responses that incorporates top-hat nonlocal perception and parasitic time delay. Theoretically, we have analyzed the conditions for the occurrence of Turing bifurcation, Hopf bifurcation, and Turing-Hopf bifurcation in the system. In numerical simulations, parameters with practical biological significance have been adopted to verify the theoretical results. The simulations have shown that the perception intensity η and perception range R jointly induce Turing bifurcation, the parasitic time delay τ can induce Hopf bifurcation, and their synergistic effect leads to Turing-Hopf bifurcation, exhibiting rich spatiotemporally coupled dynamical behaviors. Based on the above findings, this paper has proposed quantitative management strategies to avoid harmful instability by regulating the perception range R of natural enemies and optimizing release timing, which provides a theoretical basis for developing precise and stable biological control technologies. Future research can collaborate with ecological researchers to further calibrate the model by combining field monitoring data, and expand it to incorporate environmental noise, spatial heterogeneity, and other factors, so as to improve the predictive ability of the model and better serve production practice.

Use of AI tools declaration

The authors declare they have not used Artificial Intelligence (AI) tools in the creation of this article.

Acknowledgments

This study was funded by the National Natural Science Foundation of China (Grant No. 12571525) and the Northeast Forestry University College Student Innovation and Entrepreneurship Training Program Project (DCLXY-202613).

Conflict of interest

The authors declare there are no conflicts of interest.

References

1. W. Wu, Z. Zhang, L. Zheng, C. Han, X. Wang, J. Xu, et al., Research progress on the early monitoring of pine wilt disease using hyperspectral techniques, *Sensors*, **20** (2020), 3729. https://doi.org/10.3390/s20133729
2. Y. Zheng, Z. Yang, X. Wang, Mechanism of chemical ecology of Bursaphelenchus xylophilus vectored by Monochamus alternatus, *Plant Prot.*, **40** (2014), 12–15. https://doi.org/10.3969/j.issn.0529-1542.2014.01.002
3. X. Wang, Y. Cao, L. Wang, C. Piao, C. Li, Current status of Pine Wilt Disease and its control status, *J. Environ. Entomol.*, **40** (2018), 256–267.
4. Y. Yang, Z. Yang, X. Wang, J. Yu, X. Yan, Predation and parasitism of Sclerodermus sp. (Hymenoptera: Bethylidae) on the young larvae of Monochamus alternatus (Coleoptera: Cerambycidae), *For. Res.*, **26** (2013), 312–319. https://doi.org/0.13275/j.cnki.lykxyj.2013.03.002
5. C. S. Holling, The functional response of predators to prey density and its role in mimicry and population regulation, *Mem. Entomol. Soc. Can.*, **97** (1965), 5–60. https://doi.org/10.4039/entm9745fv
6. M. Baurmann, T. Gross, U. Feudel, Instabilities in spatially extended predator-prey systems: Spatio-temporal patterns in the neighborhood of Turing-Hopf bifurcations, *J. Theor. Biol.*, **245** (2007), 220–229. https://doi.org/10.1016/j.jtbi.2006.09.036
7. J. Yang, Dynamics behaviors of a stage-structured pest management model with time delay and impulsive effects, *Math. Methods Appl. Sci.*, **44** (2021), 13116–13132. https://doi.org/10.1002/mma.7613
8. Y. Hou, Y. Ding, W. Jiang, Spatial pattern formation in pine wilt disease model with prey-taxis and nonlocal competition, *Discrete Contin. Dyn. Syst. - Ser. B*, **30** (2025), 3479–3504. https://doi.org/10.3934/dcdsb.2025030
9. Q. An, C. Wang, H. Wang, Analysis of a spatial memory model with nonlocal maturation delay and hostile boundary condition, *Discrete Contin. Dyn. Syst.*, **40** (2020), 5845–5868. https://doi.org/10.3934/dcds.2020249
10. J. Wang, X. Meng, X. Lei, Bifurcations and control for plant-herbivore systems with spatiotemporal nonlocal effects in arid regions, *Int. J. Bifurcation Chaos*, **36** (2026), 2650071. https://doi.org/10.1142/S0218127426500719
11. X. Meng, Z. Liang, Dynamics analysis of a delayed diffusive predator-prey model with memory-based diffusion and fear effect of prey, *Int. J. Biomath.*, (2026), 2550101. https://doi.org/10.1142/S1793524525501013
12. J. Wang, S. Wu, J. Shi, Pattern formation in diffusive predator-prey systems with predator-taxis and prey-taxis, *Discrete Contin. Dyn. Syst. - Ser. B*, **26** (2021), 1273–1289. https://doi.org/10.3934/dcdsb.2020162
13. S. Wu, Y. Song, Spatiotemporal dynamics of a diffusive predator-prey model with nonlocal effect and delay, *Commun. Nonlinear Sci. Numer. Simul.*, **89** (2020), 105310. https://doi.org/10.1016/j.cnsns.2020.105310

14. S. Xue, Y. Song, H, Wang, Spatio-temporal dynamics in a reaction-diffusion equation with nonlocal spatial memory, *SIAM J. Appl. Dyn. Syst.*, **23** (2024), 641–667. https://doi.org/10.1137/22M1543860

15. Y. Song, H, Wang, J. Wang, Cognitive consumer-resource spatiotemporal dynamics with nonlocal perception, *J. Nonlinear Sci.*, **34** (2024), 19. https://doi.org/10.1007/s00332-023-09996-w

16. J. Li, Y. Ding, W. Jiang, Dynamical analysis of a Pine Wilt Disease model with memory-based diffusion and nonlocal effect, *J. Math. Biol.*, **91** (2025), 6. https://doi.org/10.1007/s00285-025-02236-7

17. J. Li, Y. Ding, Y. Song, Pattern formation driven by nonlocal perception in a delayed pine wilt disease model with top-hat kernel, *Bull. Math. Biol.*, **87** (2025), 126. https://doi.org/10.1007/s11538-025-01504-3

18. Y. Zheng, Y. Wang, W. Wang, Y. Li, L. Fan, Y. Shi, et al., Parasitic effect of Dastarcus helophoroides of Monochamus alternatus biotype on Monochamus saltuarius, *Chin. J. Biol. Control*, **38** (2022), 587–594. https://doi.org/10.16409/j.cnki.2095-039x.2022.05.002

19. Y. Zhang, Z. Yang, X. Wang, Y. Zhang, C. Wu, S. Ma, et al., Functional response of the parasitoid Sclerodermus sp. (Hymenoptera: Bethylidae) to the third instar larvae of host Monochamus alternatus (Coleoptera: Cerambycidae), *Acta Entomol. Sin.*, **55** (2012), 426–434. https://doi.org/10.16380/j.kcxb.2012.04.006

20. Y. Zheng, Y. Zhang, Y. Shi, L. Fan, Y. Li, Preliminary study on the control efficiency of Monochamus saltuarius by Sclerodermus spp., *Chin. J. Biol. Control*, **38** (2022), 306–311. https://doi.org/10.16409/j.cnki.2095-039x.2021.09.030

21. W. F. Fagan, E. Gurarie, S. Bewick, A. Howard, R. S. Cantrell, C. Cosner, Perceptual ranges, information gathering, and foraging success in dynamic landscapes, *Am. Nat.*, **189** (2017), 474–489. https://doi.org/10.1086/691099

22. X. Wen, D. Song, Z. Yang, Z. Wang, M. Shi, Relationships between the emergence of Dastarcus helophoroides (Coleoptera: Bothrideridae) and the emergence of the host Monochamus alternatus (Coleoptera: Cerambycidae) in Pinus massoniana forests, *Sci. Silvae Sin.*, **56** (2020), 193–200. https://doi.org/10.11707/j.1001-7488.20200921

23. J. K. Jung, C. Lee, B. Jang, Y. Nam, Effects of sex, age, and body size on flight performance of Monochamus alternatus (Coleoptera: Cerambycidae), a vector of pine wood nematodes, using flight mills, *Insects*, **16** (2025), 444. https://doi.org/10.3390/insects16050444

AIMS Press